

DISSERTATION

IMAGING OF SINGLE BARIUM ATOMS IN SOLID XENON FOR BARIUM TAGGING IN THE
nEXO NEUTRINOLESS DOUBLE BETA DECAY EXPERIMENT

Submitted by

Timothy Walton

Department of Physics

In partial fulfillment of the requirements

For the Degree of Doctor of Philosophy

Colorado State University

Fort Collins, Colorado

Fall 2015

Doctoral Committee:

Advisor: William M. Fairbank, Jr.

Bruce Berger
Alan Van Orden
Robert Wilson

Copyright by Timothy Walton 2015

All Rights Reserved

ABSTRACT

The nEXO experiment is designed to search for zero-neutrino double beta decay of the isotope ^{136}Xe , in order to better understand the nature of neutrinos. Since the daughter of this decay is barium (^{136}Ba), detecting the presence of ^{136}Ba at a decay site (called “barium tagging”) provides an additional discriminator to reject backgrounds in the search for this decay. This would involve detecting a single barium ion from within a macroscopic volume of liquid xenon. One proposed barium tagging method is to trap the barium ion in solid xenon (SXe) at the end of a cold probe, and then detect the ion by its fluorescence in the solid xenon. The William M. Fairbank Jr. group at Colorado State University has been working toward this goal with steady success for some time. In this thesis, I demonstrate successful detection of neutral Ba in SXe down to the single atom level, after deposition from vacuum.

needs some more detail

ACKNOWLEDGEMENTS

I thank my adviser William M. Fairbank, Jr. with inadequate words for his inspiring courage, foresight, and intuition as a physicist. The success of this thesis, those to come, and of the experimental method which they work toward belongs foremost to him. Special thanks also to Chris Chambers for tireless help with experiment and analysis, and ambition to continue the work. I thank him and Adam Craycraft for companionship and intellectual input. I thank Shon Cook and Brian Mong for developing the apparatus, pioneering the work, and training me along with Cesar Benitez and Kendy Hall. I also thank the nEXO collaboration for their support, and especially their spokesman Giorgio Gratta. I thank my wife for supporting and dealing with the physicist lifestyle, and everyone in my family for inspiration and vital support.

This dissertation is typset in L^AT_EX using a document class designed by Leif Anderson.

Dedicated to my new son Logan.

TABLE OF CONTENTS

Abstract	ii
Acknowledgements	iii
Chapter 1. Introduction	1
1.1. Neutrinos	2
1.2. Double Beta Decay	6
1.3. Enriched Xenon Observatory	8
Chapter 2. Theory	19
2.1. Ba/Ba ⁺ Spectroscopy in Vacuum	19
2.2. Matrix Isolation Spectroscopy	20
2.3. 5-level System	22
2.4. Fluorescence Efficiency	22
Chapter 3. Experimental	24
3.1. Ion Beam	24
3.2. Ba Getter Source	32
3.3. Sample Deposition	32
3.4. Laser Excitation	35
3.5. Collection Optics	37
3.6. Vibrations and Effective Laser Region	39
3.7. Laser Scanning	41
Chapter 4. Results: Spectroscopy	43
4.1. Emission and Excitation of Ba in SXe	43

4.2.	619-nm Peak Identification	46
4.3.	Annealing/Temperature Dependence	47
4.4.	Bleaching	52
4.5.	Backgrounds	57
4.6.	Candidate Ba ⁺ Lines/Blue Excitation	60
Chapter 5.	Results: Imaging	65
5.1.	Imaging 577- and 591-nm peaks	66
5.2.	Imaging 619-nm peak	68
5.3.	Scanned Images	71
Chapter 6.	Conclusions	74
6.1.	Future Steps	74
Bibliography		75

CHAPTER 1

INTRODUCTION

Neutrinos have been at the forefront of discovery in physics since their prediction by W. Pauli, who proposed in 1930 the existence of a neutral, unobserved particle to explain the apparent violation of energy conservation in beta decay [1]. He admitted that neutrinos (then deemed “neutrons” – what we now know as neutrons had not been discovered yet either) should be difficult to observe experimentally, but also that it seemed unlikely that they would never have been noticed before. As it turns out, they are much more difficult to observe than he predicted; they will not be noticed without extreme experimental techniques.

A theory formulated in 1933 by E. Fermi for beta decay [2], including the neutrino, would be the beginnings of weak interaction theory, and the development of the very successful Standard Model (SM) of particle physics. However, the SM assumes that neutrinos are massless. The discovery of non-zero neutrino mass via neutrino oscillations in the late 1990s [3] shows that there is more new physics to be discovered, and presents a path to follow.

Neutrinos are difficult to study, but the rewards are profound. The See-saw Mechanism is a theory which predicts the extreme lightness of neutrinos, while also predicting very heavy neutrino partners. The existence of heavy neutrinos in the high-energy environment of the early universe, coupled with the possibility of the violation of CP conservation which could slightly favor the production of matter vs. anti-matter in decays of these heavy neutrinos, could explain why the universe became dominated by matter. [4]

If this theory is correct, then neutrinos would be described by the Majorana formulation rather than Dirac, and the process of neutrinoless double beta decay ($0\nu\beta\beta$) would be allowed. Observation of $0\nu\beta\beta$ would simultaneously demonstrate that neutrinos are Majorana

particles, as well as aid in determining the absolute mass itself [5]. This chapter outlines the current theory for neutrinos, and then describes the $0\nu\beta\beta$ experiments EXO-200 and nEXO, in order to motivate barium tagging for nEXO.

1.1. NEUTRINOS

Neutrinos are chargeless leptons which only interact via the weak force (and gravity). There are three known “flavors” of neutrinos, ν_e , ν_μ , and ν_τ , each corresponding to one of the three known leptons. These are the eigenstates in the basis of the weak force, so they are the states in which a neutrino will interact via the weak force.

1.1.1. NEUTRINO OSCILLATION AND MASS

The postulate that neutrinos have an energy basis which is different from the flavor basis predicts the phenomenon of oscillation – that the time evolution of an initially pure flavor state (as a neutrino will be produced) will result in a time-dependent probability of measuring the other two flavors as well.

The very small mass of a neutrino (assumed zero in the SM), specifically relative to its momentum, lets one write its Hamiltonian in terms of mass squared differences $\Delta m_{ij}^2 = m_i^2 - m_j^2$, where $i,j = 1,2,3$, referring to what we then call mass states. The mass basis is really the energy basis with the small mass approximation, along with dropping some constant terms in the Hamiltonian (which do not affect time evolution).

The mixing between the 3-vector mass and flavor bases is defined by a rotation in terms of three mixing angles, θ_{12} , θ_{23} , and θ_{13} . Transformation between the flavor and mass bases is done with the following unitary matrix, called the Pontecorvo–Maki–Nakagawa–Sakata (PMNS) matrix [6]:

$$\begin{aligned}
(1) \quad U &= \begin{pmatrix} 1 & 0 & 0 \\ 0 & c_{23} & s_{23} \\ 0 & -s_{23} & c_{23} \end{pmatrix} \begin{pmatrix} c_{13} & 0 & s_{13}e^{-i\delta} \\ 0 & 1 & 0 \\ -s_{13}e^{i\delta} & 0 & c_{13} \end{pmatrix} \begin{pmatrix} c_{12} & s_{12} & 0 \\ -s_{12} & c_{12} & 0 \\ 0 & 0 & 1 \end{pmatrix} \begin{pmatrix} 1 & 0 & 0 \\ 0 & e^{i\alpha_1/2} & 0 \\ 0 & 0 & e^{i\alpha_2/2} \end{pmatrix} \\
&= \begin{pmatrix} c_{12}c_{13} & s_{12}c_{13} & s_{13}e^{-i\delta} \\ -s_{12}c_{23} - c_{12}s_{23}s_{13}e^{i\delta} & c_{12}c_{23} - s_{12}s_{23}s_{13}e^{i\delta} & s_{23}c_{13} \\ s_{12}s_{23} - c_{12}c_{23}s_{13}e^{i\delta} & -c_{12}s_{23} - s_{12}c_{23}s_{13}e^{i\delta} & c_{23}c_{13} \end{pmatrix} \begin{pmatrix} 1 & 0 & 0 \\ 0 & e^{i\alpha_1/2} & 0 \\ 0 & 0 & e^{i\alpha_2/2} \end{pmatrix}
\end{aligned}$$

where $c_{ij} = \cos \theta_{ij}$ and $s_{ij} = \sin \theta_{ij}$. δ and α_i are Dirac and Majorana, respectively, CP-violating phases. Transformation between bases is done by Eqn. 2:

$$\begin{aligned}
(2) \quad |\nu_\alpha\rangle &= \sum_i U_{\alpha i}^* |\nu_i\rangle, \\
|\nu_i\rangle &= \sum_\alpha U_{\alpha i} |\nu_\alpha\rangle.
\end{aligned}$$

A two-neutrino approximation demonstrates how this results in neutrino oscillation. In this case, there is only one mixing angle θ and one mass squared difference Δ , and the Hamiltonian H and mixing matrix U are as follows:

$$\begin{aligned}
(3) \quad H &= \frac{1}{4E} \begin{pmatrix} -\Delta & 0 \\ 0 & \Delta \end{pmatrix} \\
U &= \begin{pmatrix} \cos \theta & \sin \theta \\ -\sin \theta & \cos \theta \end{pmatrix}.
\end{aligned}$$

Applying time evolution to, say, a pure electron neutrino (where the two neutrino flavors here are ν_e and ν_μ) then leads to the following state:

$$(4) \quad \begin{aligned} |\nu_e(t)\rangle &= (e^{it\Delta/4E} \cos^2 \theta + e^{-it\Delta/4E} \sin^2 \theta) |\nu_e(0)\rangle \\ &\quad + \cos \theta \sin \theta (-e^{it\Delta/4E} + e^{-it\Delta/4E}) |\nu_\mu(0)\rangle \end{aligned}$$

where E is the neutrino energy. Note that if θ is zero, the case where the mass basis is the same as the flavor basis, the state remains pure ν_e . The same is true if Δ is zero. Thus, the discovery of neutrino oscillation, i.e. the discovery of mixed amplitudes in propagation equations like Eqn. 4, was the first (and only, so far) demonstration that neutrinos have a non-zero mass (*particularly a non-zero mass squared difference*).

Studying oscillations of neutrinos from different kinds of sources, with different energies and path lengths, can isolate sensitivities to the different mixing angles and mass squared differences. For example, the study of solar neutrinos (neutrinos emanating from nuclear fusion reactions in the core of the sun) provides sensitivity to θ_{12} and Δm_{12}^2 . The oscillation parameters so far measured are shown in Table 1.1.

TABLE 1.1. Best-fit values for neutrino oscillation parameters, from a global fit to oscillation experiment data. Parameters which depend on the mass hierarchy have values for NH (IH). The atmospheric parameter Δm^2 is defined as $\Delta m^2 = \Delta m^2 = \Delta m_{31}^2 - \Delta m_{21}^2/2 > 0$ ($\Delta m^2 = \Delta m_{32}^2 + \Delta m_{21}^2/2 < 0$). [6]

Parameter	Measurement ($\pm 1\sigma$)
Δm_{12}^2	$7.54_{-0.22}^{+0.26} 10^{-5} \text{ eV}^2$
$ \Delta m^2 $	$2.43 \pm 0.06 (2.38 \pm 0.06) 10^{-3} \text{ eV}^2$
$\sin^2 \theta_{12}$	0.308 ± 0.017
$\sin^2 \theta_{23}$	$4.37_{-0.023}^{+0.033} (4.55_{-0.031}^{+0.039})$
$\sin^2 \theta_{13}$	$0.0234_{-0.0019}^{+0.0020} (0.0240_{-0.0022}^{+0.0019})$
δ/π (2σ range)	$1.39_{-0.27}^{+0.38} (1.31_{-0.33}^{+0.29})$



FIGURE 1.1. The two possible hierarchies of neutrino masses. The colors depict the mixing between the mass and flavor bases.

Note that only the absolute value of the atmospheric neutrino oscillation parameter Δm^2 is known. As a consequence, there are two possibilities for the hierarchy of the three neutrino masses. These are called the Normal and Inverted Hierarchies, as shown in Fig. 1.1. The correct mass hierarchy remains unknown, but next-generation neutrino experiments, possibly including nEXO, may be able to discern this.

Neutrino oscillation demonstrates that neutrinos have non-zero mass, and though oscillation experiments measure the mass squared differences, the absolute masses of the three neutrinos remain unknown. Cosmology can put limits on the sum of the three neutrino masses. The Planck collaboration reports an upper bound on this sum at $\sum_i m_i < 0.23 \text{ eV}$ [7]. The KATRIN experiment will search for absolute neutrino mass with sensitivity of $m_{\bar{\nu}_e} < 0.2 \text{ eV}$ (90% CL) by measuring the spectrum of tritium beta decay near the Q-value (maximal decay energy) [8].



FIGURE 1.2. Two-neutrino (left) and neutrinoless (right) double beta decay.

1.2. DOUBLE BETA DECAY

Double beta decay is the simultaneous decay of two neutrons in a nucleus into two protons and two electrons. Two-neutrino double beta decay ($2\nu\beta\beta$), shown in Fig. 1.2(left), is allowed by the Standard Model and has been observed in eleven isotopes with half-lives between 10^{19} and 10^{21} years. Similar to beta decay, a neutrino accompanies each electron in this decay, broadening the spectrum of the summed electron energy. This is a second-order process, making it a rare decay, and requiring low backgrounds to measure.

$0\nu\beta\beta$, shown in Fig. 1.2(right), is a postulated mode of double beta decay. In this case, the neutrino is exchanged as a virtual particle (which would require that it is a Majorana particle), and there are no neutrinos in the final products. If discovered, not only would neutrinos be determined to be Majorana particles, but the measured $0\nu\beta\beta$ half-life would also aid in determining absolute neutrino mass according to Eqn. 5:

$$(5) \quad T_{1/2}^{0\nu} = (G^{0\nu}(Q, Z)|M^{0\nu}|^2 \langle m_\nu \rangle^2)^{-1}$$



FIGURE 1.3. Conceptual two-neutrino (blue) and zero-neutrino (red) double beta decay spectra.

where $T_{1/2}^{0\nu}$ is the $0\nu\beta\beta$ half-life, $G^{0\nu}$ is a known phase space factor, and $M^{0\nu}$ is a model-dependent nuclear matrix element. $\langle m_\nu \rangle$ is the effective Majorana neutrino mass:

$$(6) \quad \langle m_\nu \rangle = \sum_i U_{ei}^2 m_i.$$

The sum of the energies of the emitted electrons in double beta decay will serve as the distinction between the two-neutrino and zero-neutrino modes, shown in Fig. 1.3. In the two-neutrino mode, the total decay energy is shared probabilistically between the electrons and the neutrinos (the nuclear recoil energy is negligible), resulting in a broad distribution in the summed electron energy. (Recall the similarly broad electron energy in single beta decay, which ultimately led to discovery of the neutrino involved.) But in the zero-neutrino mode, essentially all of the decay energy is carried away by the two electrons, resulting in only a single allowed value for the summed electron energy – a peak in the summed electron energy spectrum at the Q-value.

The rarity of double beta decay requires very low backgrounds, especially around the Q-value for the $0\nu\beta\beta$ search. The next sections describe the experiments EXO-200 and its next-generation successor, nEXO.

1.3. ENRICHED XENON OBSERVATORY

EXO-200 and nEXO (EXO standing for Enriched Xenon Observatory) are a progression of two experiments, each a liquid xenon (LXe) time projection chamber (TPC) designed to study the double beta decay of the isotope ^{136}Xe , and ultimately to search for the zero-neutrino mode. ^{136}Xe is fairly unique among the double beta decay isotopes in that it can be studied in a gas or liquid TPC instead of solid crystals or foils. The 3D event position reconstruction abilities of a TPC have advantages in background reduction, described in section 1.3.1. Purification of Xe is straightforward and can be done continuously in a detector. LXe is transparent, and produces substantial ionization and scintillation at 178 nm when energy is deposited in the LXe [9]. A liquid TPC approach also offers the opportunity to identify, or “tag”, the daughter $^{136}\text{Ba}^{++}$ at the site of the double beta decay event, which would provide a method for background-free identification of $0\nu\beta\beta$ [10]. Barium tagging is the focus of our group at CSU and is the subject of this thesis. The following sections describe the EXO-200 experiment, as well as nEXO, the next-generation tonne-scale LXe TPC, which is now in the research and development stage. EXO-200 does not have barium tagging implemented, but it is hoped that nEXO will.

1.3.1. EXO-200

Located about half a mile underground in the Waste Isolation Pilot Plant (WIPP) near Carlsbad, NM, EXO-200 has been operational since 2011. It is a TPC using LXe enriched



FIGURE 1.4. Drawing of EXO-200 TPC Vessel with surrounding cryostat, lead walls, and muon veto panels.

to $80.672\% \pm 0.14\%$ ^{136}Xe [9], with a fiducial volume corresponding to 66.20 kg of ^{136}Xe .

It is designed to probe Majorana neutrino masses down to around 109-135 meV (the range covers different matrix element calculations) [11]. The WIPP mine is in a salt basin, which contains lower levels of Uranium and Thorium than rock in a typical mine.

A schematic diagram of the TPC in the class 100 cleanroom is shown in Fig. 1.4. Several layers of lead wall surround the copper cryostat, which is filled with HFE-7000, a cryogenic fluid which keeps the TPC cooled to LXe temperatures, as well as aids in shielding the detector. The TPC vessel is made of low-radioactivity copper, and is kept as thin as possible to minimize backgrounds. Scintillating panels on the outside of the cleanroom provide a cosmic ray muon veto.



FIGURE 1.5. EXO-200 TPC cutaway view [9].

A cut-away view of the EXO-200 detector is shown in Fig. 1.5. It is two mirrored TPCs which share a cathode. The detection planes are a combination of ionized charge induction/collection wires and large area avalanche photodiodes (LAAPDs), which detect scintillation light [12].

A view into one of the TPCs is shown in Fig. 1.6. On the detection plane, holes for the LAAPDs can be seen below the cross-hatched u- and v-wires. The white material on the inner wall is the Teflon reflector. When a double beta decay event occurs in the LXe,

the energetic electrons ionize many surrounding Xe atoms, as well as produce a scintillation signal. Scintillation light provides an initial time for z-measurement of the event, as well as an energy measurement.

The cathode is set to -8 kV, providing an electric field of 374 V/cm across the 20 cm drift length of each TPC. Ionized electrons drift from the decay site, first passing the v-wires, which receive an induction signal, and are then collected by the u-wires, which are set at a 60° angle from the v-wires, as depicted in Fig. 1.7. An electric field of 778 V/cm between the u- and v-wires ensures 100% v-wire transparency. The charge collection provides an energy measurement complimentary to that of the scintillation. Together, the u- and v-wires give an x/y position measurement for the event. The time between the initial scintillation detection and the charge collection give a z position. Thus a 3D position can be reconstructed for the event if u-wire, v-wire, and scintillation signals are detected. [9]

Having a reconstructed 3D event position is important in several ways. Firstly, position-based corrections to scintillation and charge collection can be applied. For charge, electronegative impurities in the LXe will absorb the drifting charge, requiring a drift-length (z-position) correction. High purity levels, measured in terms of electron lifetime, of $2\text{--}3 \times 10^3$ μs and higher are maintained in EXO-200, resulting in a small correction of a few % for maximal drift lengths. For scintillation, a 3D correction is applied, as some regions have more efficient light collection by the LAAPDs. A 3D position also allows a fiducial volume to be defined. A standoff distance from detector surfaces aids in distinction between gamma ray events and double beta decay events, as gamma interactions tend to occur on detector materials, while double beta decay are uniformly distributed in the LXe. Gamma



FIGURE 1.6. View of the detection plane in one of the two EXO-200 TPCs.

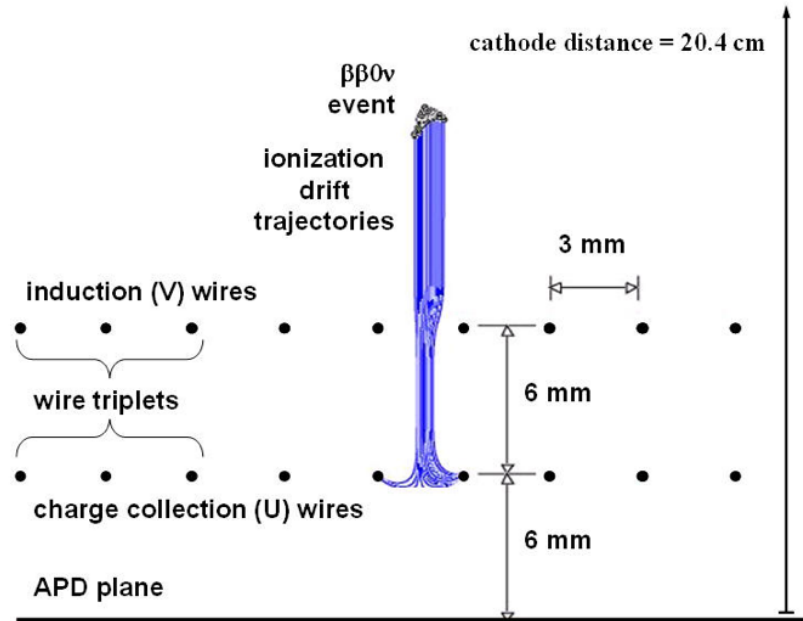


FIGURE 1.7. EXO-200 event topology.

rays also exhibit some attenuation in the LXe. Finally, 3D reconstruction allows the distinction between single-site (SS) and multi-site (MS) events. A MS event is one where two spatially separated events occur in the same $2048\text{-}\mu\text{s}$ time window. These are mostly caused by gamma events, which can Compton-scatter several times in the LXe. Rejecting MS events further aids in separating gamma events from double beta decay events. [9] Barium tagging will also benefit from a 3D reconstructed position in nEXO.

The final data set is fit using a combination of probability distribution functions (PDFs) for $0\nu\beta\beta$, $2\nu\beta\beta$, and background components. Fits to the final energy spectrum data for (a) SS events, and (b) MS events are shown in Fig. 1.8 for the most recent $0\nu\beta\beta$ analysis. The green bands beneath each plot show the residuals vs. energy. The $2\nu\beta\beta$ spectrum, in gray, dominates the signal in the SS spectrum below the Q-value. The vertical red lines in the SS spectrum outline the $\pm 2\sigma$ region of interest around the Q-value, where the $0\nu\beta\beta$ peak will lie. The insets are a zoom into this region. The fit value for $0\nu\beta\beta$ in this dataset is non-zero, but it is consistent with the null hypothesis at 1.2σ . This sets an upper limit on the $0\nu\beta\beta$ half-life at $T_{1/2}^{0\nu\beta\beta} < 1.1 \times 10^{25}$ yr (90% CL), which corresponds to $\langle m_{\nu_e} \rangle < 190\text{-}450$ meV depending on nuclear matrix element calculations [14]. EXO-200 reports the $2\nu\beta\beta$ half-life measurement in [9] of $T_{1/2}^{2\nu\beta\beta} = 2.165 \pm 0.016(\text{stat}) \pm 0.059(\text{sys}) \times 10^{21}$ yr. This is more precise but consistent with previous measurements by EXO-200 in 2011 [15] and KamLAND-ZEN in 2012 [16].

1.3.2. nEXO

The next-generation successor to EXO-200 is nEXO, a tonne-scale LXe TPC which will probe Majorana neutrino masses down to the 10 meV scale. The sensitivity projections for nEXO are shown in Fig. 1.9, along with those of EXO-200. nEXO will reach phase space



FIGURE 1.8. EXO-200 energy spectrum from $0\nu\beta\beta$ search analysis [14].

where the two possible mass hierarchies split, and will probe the full phase space of the inverted hierarchy. Barium tagging will push the sensitivity further into the region allowed only by the normal hierarchy.

A schematic diagram of the nEXO in the SNOLAB cryopit, one of the possible locations for nEXO, is shown in Fig. 1.10. Similar to EXO-200, the copper-housed TPC will be submerged in HFE fluid, inside a copper cryostat. The cryostat will be insulated and submerged in a large volume of water shielding, in which photo-multiplier tubes could provide muon veto by observing Cherenkov radiation. nEXO will be a single TPC with charge and light



FIGURE 1.9. nEXO projected sensitivity to the Majorana neutrino mass vs. the minimum of the three masses m_{min} . Solid (dotted) lines are $1(2)\sigma$ bands on measured neutrino oscillation parameters. [can I have this in here?](#)

readouts at opposing ends of the TPC. Rather than wires, nEXO will use tile electrodes for charge readout, shown in Fig. 1.11. Silicon photo-multipliers will be used for light detection.

1.3.3. BARIUM TAGGING

The ability to observe the daughter of each $0\nu\beta\beta$ event is the ultimate background rejection technique. Several possible barium tagging techniques have been proposed for nEXO. The original and most natural concept is to direct one or more lasers at the decay



FIGURE 1.10. nEXO TPC in the SNOLAB cryopit.



FIGURE 1.11. nEXO readout.

site to induce fluorescence of the barium daughter [10]. This technique was explored by the Fairbank group, and was abandoned when Ba^+ fluorescence could not be confidently observed in LXe [17].

A few barium tagging techniques continue to be explored. One of these is to grab the daughter on a probe surface, brought to the decay site by a probe. It would then be moved to a location where it can be desorbed from that surface by an infrared laser, and subsequently resonantly ionized by two lasers in order to detect it by time-of-flight spectroscopy. The apparatus for the study of this method is described in [18], along with some initial results.

The other remaining technique for barium tagging, now the focus of the Fairbank group and the subject of this thesis, is called tagging in SXe. Here, a cold probe would go to the site of the candidate $0\nu\beta\beta$ event in order to trap the Ba/Ba^+ in a small amount of SXe, and then observe it by its laser-induced fluorescence in the SXe, a technique called matrix isolation spectroscopy. A concept for a probe is shown in Fig. 1.12. The SXe forms on a sapphire window at the end of the probe. Sapphire is a good candidate for a substrate because it has good thermal conductivity at low temperature and is highly transparent. An excitation laser would be brought into the probe through a fiber, and aimed through the sapphire to excite the Ba/Ba^+ in the SXe. A return fiber could collect the laser reflections to measure the SXe thickness via interference fringes. The Ba/Ba^+ fluorescence would then be collected by a lens/filter system and imaged onto a CCD. Additional components, not shown, would be required for cooling the sapphire, either by liquid He or by a Joule-Thompson nozzle, as well as a thermometer.

Whether the daughter Ba will neutralize or remain ionized is not yet known. It is however expected that a Ba^{++} ion will neutralize at once to Ba^+ by charge transfer in LXe, since the



FIGURE 1.12. Concept for a cryoprobe containing excitation/collection optics.

LXe conduction band gap is slightly less than the ionization potential for Ba^+ [10]. Further neutralization by recombination with the electron cloud could also occur. However, a study of neutralization of beta decay daughters in EXO-200 has observed a high percentage, 76(5)%¹, of ionized daughters [ref alphaion]. This provides some expectation of a high percentage of ionized $0\nu\beta\beta$ daughters.

CHAPTER 2

THEORY

2.1. BA/BA⁺ SPECTROSCOPY IN VACUUM

The lowest-lying energy levels in vacuum for Ba and Ba⁺ are shown in Fig. 2.1. For Ba, the main transition is between the ground $6s^2 \ ^1S_0$ to the excited $6s6p \ ^1P_1^o$ state, however branching ratios from the P state result in a decay to one of three metastable D states in about 1 in 330 excitations. For Ba⁺, two strong transitions exist between the ground $6s \ ^2S_{1/2}$ and the $6p \ ^2P_{1/2}$ and $6p \ ^2P_{3/2}$ excited states. Transitions to the two metastable D states are higher than for the atom, resulting in a decay into a D state after about 4 excitations. These D states are metastable because they are parity-forbidden to decay back to the ground state, resulting in much lower decay rates. These rates are shown in Table 2.1 along with each of the allowed transitions in Fig. 2.1.

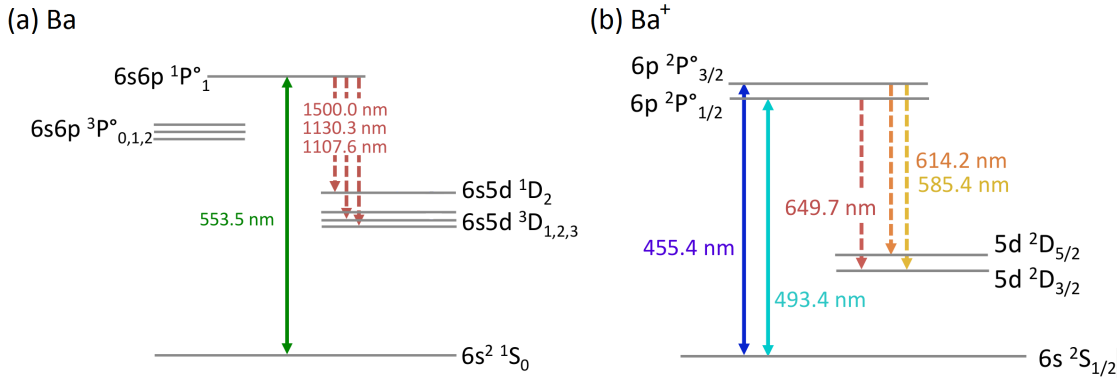


FIGURE 2.1. Energy level diagrams for (a) Ba and (b) Ba⁺.

Single atom/ion detection by spectroscopy generally requires, in addition to the main excitation laser, lasers to provide transitions out of the metastable D states once the atom/ion decays into one of them. For the atom, this can be done via three additional infrared lasers for the direct transitions back to the $6s6p \ ^1P_1^o$ state, and also via excitation to higher-level states

TABLE 2.1. *the 5-s one is 8 s for measurement in [11] of phys rev a 46 5 (1992), is 1/lifetime is right.*

	Transition	Rate (s^{-1})	Ref.
Ba	$6s6p \ ^1P_1^o \rightarrow 6s^2 \ ^1S_0$	1.19×10^8	[21]
	$6s6p \ ^1P_1^o \rightarrow 6s5d \ ^1D_2$	2.50×10^5	[21]
	$6s6p \ ^1P_1^o \rightarrow 6s5d \ ^3D_2$	1.1×10^5	[21]
	$6s6p \ ^1P_1^o \rightarrow 6s5d \ ^3D_1$	3.1×10^3	[21]
	$6s5d \ ^1D_2 \rightarrow 6s^2 \ ^1S_0$	5	[?]
	$6s5d \ ^3D_2 \rightarrow 6s^2 \ ^1S_0$	1.4^{-2}	[?]
	$6s5d \ ^3D_1 \rightarrow 6s^2 \ ^1S_0$	1.7^{-2}	[?]
Ba^+	$6p \ ^2P_{3/2}^o \rightarrow 6s \ ^2S_{1/2}$	1.11×10^8	[21]
	$6p \ ^2P_{1/2}^o \rightarrow 6s \ ^2S_{1/2}$	9.53×10^7	[21]
	$6p \ ^2P_{3/2}^o \rightarrow 5d \ ^2D_{5/2}$	4.12×10^7	[21]
	$6p \ ^2P_{3/2}^o \rightarrow 5d \ ^2D_{3/2}$	6.00×10^6	[21]
	$6p \ ^2P_{1/2}^o \rightarrow 5d \ ^2D_{3/2}$	3.10×10^7	[21]
	$5d \ ^2D_{5/2} \rightarrow 6s \ ^2S_{1/2}$	3.8×10^{-2}	[22]
	$5d \ ^2D_{3/2} \rightarrow 6s \ ^2S_{1/2}$	1.3×10^{-2}	[23]

which have paths back into the fluorescence cycle, such as $6s6p \ ^3D_1^o$. Trapping/detection of Ba atoms in a magneto-optical trap (MOT) was achieved in [24]. Observation of trapped single Ba^+ ions requires only two lasers if the $^2P_{1/2}$ excited state is used, e.g. [25].

2.2. MATRIX ISOLATION SPECTROSCOPY

In the matrix isolation spectroscopy technique [26], the species of interest, e.g. Ba/Ba^+ , is embedded and trapped in an inert host matrix, e.g. solid Xe, ideally with a host:guest ratio of 10^3 or greater for a low probability of guest-guest interaction. The ground S state of Ba, as well as for Ba^+ , is spherically symmetric, and being slightly larger in Van der Waals radius than Xe, it is likely to take the place of one or more Xe atoms in the fcc crystal (substitution), vs. existing in between Xe atoms in the crystal structure (interstitial). However, the strength of the Ba-Xe interaction, an induced dipole-dipole Van der Waals force, is quite different when the Ba is in the non-spherically-symmetric excited P state [27]. This leads to significant broadening of absorption and emission for the Ba, as well as an energy shift between the

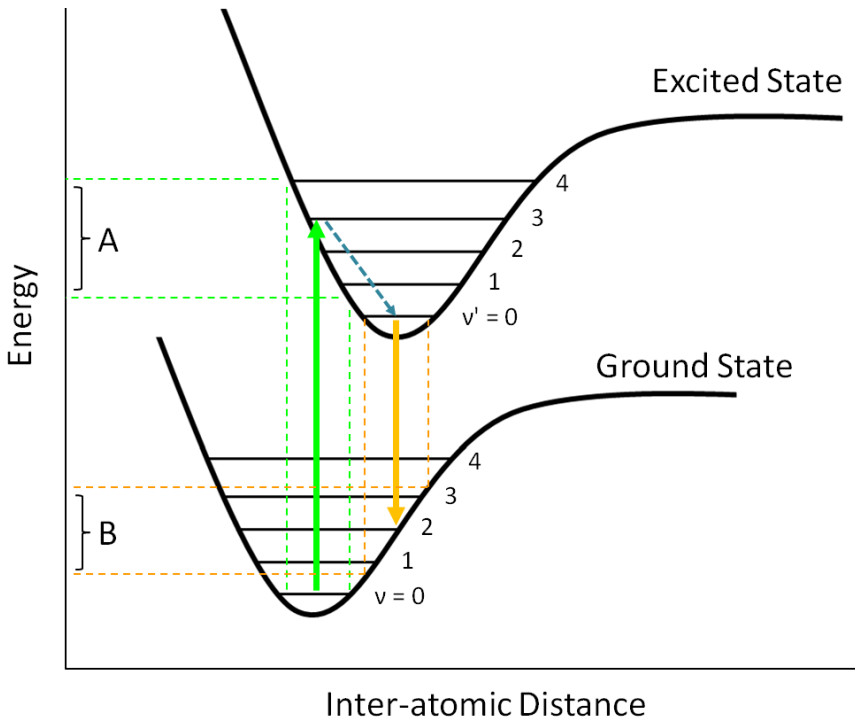


FIGURE 2.2. Illustration of the Franck-Condon Principle resulting in red-shifted emission as well as broadening in absorption (A) and emission (B) due to vibrational modes ν (ν') in the ground (excited) state.

two, according to the Franck Condon Principle, illustrated in Fig. 2.2. In a cold matrix, the system will be in the ground lattice vibrational state ($\nu = 0$) before excitation. Electronic excitation can occur to multiple vibrational modes whose wavefunctions overlap that of the ground state, thus broadening the absorption energy. In the excited state, rapid decay occurs to the lowest vibrational mode, and then a similar broadening in the spontaneous emission energy occurs. A redshift in the emission is observed relative to the excitation.

The spectroscopy of Ba in solid Ar (SAr) and solid Kr (SKr) matrices was studied in [28]. The example of Ba in SAr is shown in Fig. 2.3. The absorption is 10s of nm broad with a multi-peak structure, and the emission is broadened to nms and red-shifted. These were attributed to the main $6s^2 \ ^1S_0 \rightarrow 6s6p \ ^1P_1^o$ transition and its spontaneous emission.

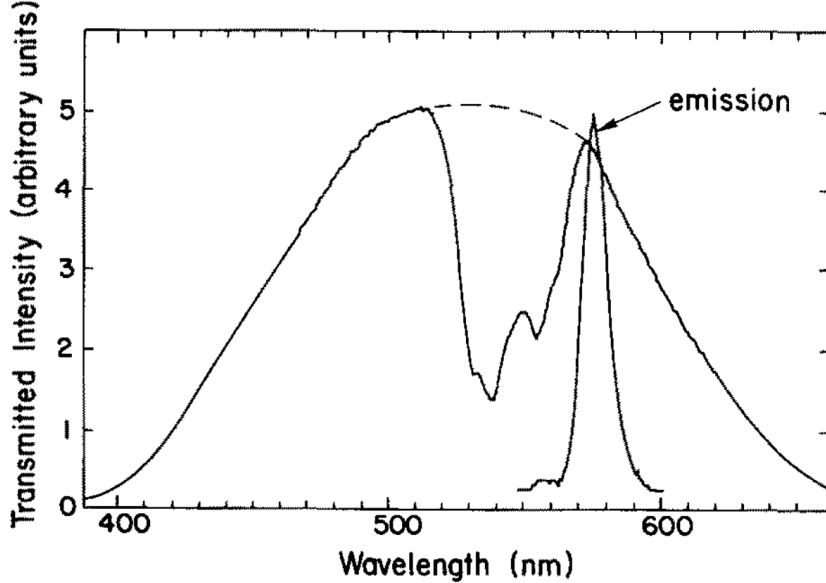


FIGURE 2.3. Absorption and emission spectra of neutral Ba in SAr at 10 K. [28]

Energy level transition probabilities can also be affected in a matrix, e.g., spin-forbidden transitions can become more significant via the heavy atom effect. If electronic potential energy curves cross each other, non-radiative transitions can become allowed for otherwise forbidden transitions. [27] Effects like these could aid in observation of the Ba/Ba⁺, e.g. by improving decay rates out of metastable D states, or they could reduce detectability, e.g. if a non-radiative decay competes with the fluorescence channel.

2.3. 5-LEVEL SYSTEM

2.4. FLUORESCENCE EFFICIENCY

Fluorescence efficiency, ϵ_f , is the ratio of fluorescence photons emitted to excitations into the fluorescing state. This becomes less than one when there are paths out of the excited state other than the one which emits the photon being measured, e.g. the ϵ_f of Ba in vacuum is about 99.7%, not quite 1 due to about 1 in 330 decays from the P state into a metastable D state rather than back to ground. ϵ_f can be calculated by Eqn. 7:

$$(7) \quad \epsilon_f = \frac{f}{w_{12}\epsilon_c} = \frac{fh\nu}{\sigma I \epsilon_c}$$

where f is the number of fluorescence photons observed per atom, w_{12} is the excitation rate, ϵ_c is the collection efficiency of the system, σ is the cross section for the excitation interaction, I is the laser intensity, and $h\nu$ is the excitation photon energy. σ can be measured by experiment, and the remaining parameters are easily calculated to produce a measurement of ϵ_f .

CHAPTER 3

EXPERIMENTAL

This chapter describes the apparatus at Colorado State University which has been used for producing and observing deposits of Ba/Ba⁺ in SXe. The main barium source, a Ba⁺ ion beam, is first described, as well as a neutral Ba getter source. The co-deposit of Ba/Ba⁺ with Xe gas onto a cold sapphire window, subsequent laser excitation, and finally the collection optics for the fluorescence are described.

3.1. ION BEAM

The ion beam system is shown in Fig. 3.1. This is a clean source of Ba⁺ which can do a very wide range of deposit sizes, from billions of ions in a focused laser region all the way down to the single-ion level and below.

3.1.1. ION SOURCE

Ba⁺ ions are produced in a Model DCIS-101 Colutron ion gun system [29]. The source is shown in Fig. 3.2. A solid barium charge is placed into the hollowed end of a stainless steel rod, which is inserted into the discharge chamber, where it is heated by a filament. The barium vaporizes, and escapes the hollowed rod around a loosely threaded set screw. The source is designed to produce a discharge between the anode plate and the filament cathode, through an argon buffer gas leaked into the source chamber. This controlled discharge would then also ionize atoms from the solid charge to produce the desired ion beam, and Ar ions would be filtered out. However, to avoid contamination of the SXe matrix with residual Ar gas, the buffer gas is not used in this work. We are still able to maintain a discharge with the residual Ba vapor. The longevity of ion current from a single charge (at least several 10s

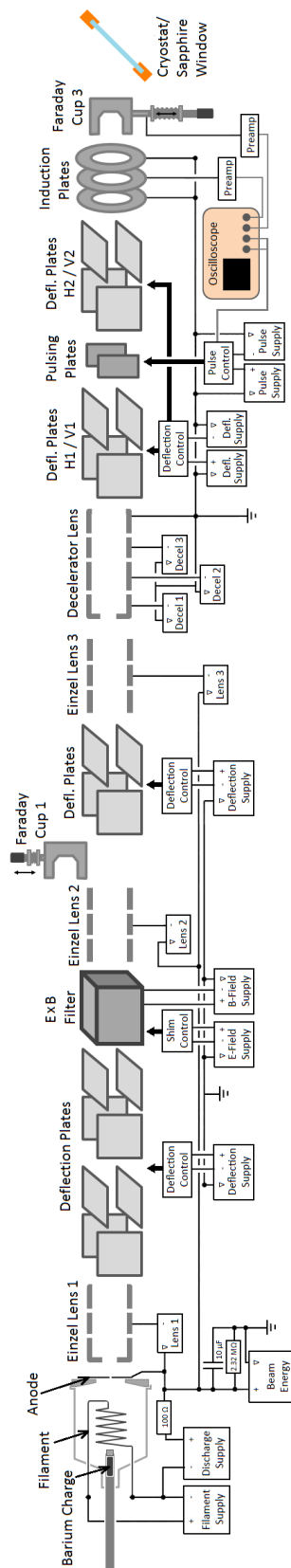


FIGURE 3.1. Ba^+ ion beam.



FIGURE 3.2. Ba^+ / Ar^+ ion source.

of hours) suggests that Ba is coating the inner walls of the source chamber, and is heated enough to provide sufficient Ba pressure to support a discharge. The discharge produces a plasma, containing barium ions, which escapes the chamber through a small hole in the anode, where it enters the acceleration region. The acceleration potential applied is 2 kV, between the ion source anode and the first element of Einzel lens 1. This lens approximately collimates the ion beam for passage through the $E \times B$ velocity filter.

3.1.2. $E \times B$ VELOCITY FILTER

The $E \times B$ velocity filter selects Ba^+ by creating perpendicular electric and magnetic fields, which produce opposing forces on charged particles moving through the filter. The opposing forces will be equal for ions with velocity $v = \frac{E}{B}$. Since ion velocity is determined by mass (m), charge (q) and beam potential (V), the filter selects ions satisfying Eqn. 8:

$$(8) \quad \frac{m}{q} = \frac{2VB^2}{E^2}$$

where B and E are the magnetic and electric fields, respectively. Those fields are chosen such that Ba^+ ions pass straight through. Other ions will be deflected.

The $E \times B$ filter is shown in Fig. 3.3. Electromagnets provide the vertical magnetic field. Electrode plates and field-shaping guard rings provide the horizontal electric field. The guard rings prevent a lensing and astigmatism effect from fringe fields of the plates [29].



FIGURE 3.3. Colutron $E \times B$ ion velocity filter.

3.1.3. OTHER BEAM COMPONENTS

The first three sets of deflection plates can be used for beam diagnostics, and are set to 0 V during normal operation. The deflection plates just before the pulsing plates, H1 and

V1, are set to constant values of +50 V and 0 V, respectively, which have been selected such that the beam, in both pulsing and continuous modes, can be deposited at the sapphire window for reasonable settings on the final deflection plates, H2 and V2. As described in Section 3.1.5, different settings in H2/V2 are required for peak ion current in Faraday cup 3 vs. peak deposit at the window.

Einzel lens 2 focuses the beam to pass through the aperture in the first element of the decelerator lens. Einzel lens 3 is set to zero in this setup. The decelerator lens can be used to vary Ba⁺ deposit energy, which was done in [30], but in this work it acts as an Einzel lens with only the second element at voltage. It focuses the beam near the sample and Faraday cup 3 (there is no Faraday cup 2 in this setup). Faraday cup 3 measures the ion current during experiments, and is retracted when deposits are being made. Calibration of deposits using Faraday cup 3 is described in Section 3.1.5. Faraday cup 1 is used for beam diagnostics, and is usually retracted.

on from ion beam studies back when? At least the procedure for alignment?

3.1.4. ION BEAM PULSING

When running in pulsing mode, the pulsing plates are normally set to 200 V and -200 V to deflect the beam, and are pulsed to 0 V for 1 μ s to pass a short pulse of ions straight forward. The pulsing circuit is shown in Fig. 3.4. Square waves, triggered by LabVIEW at 500 Hz, enter the circuit at (a). The transformed pulse triggers the MOSFET switch, which closes the circuit for the period of the pulse.

The induction plates are used to observe pulses during a deposit. Pulses just prior to a deposit can be observed by cup 3 (as well as the induction plates) for a measurement of ion current in the pulses. eV Products pre-amplifiers convert the ion current to voltage

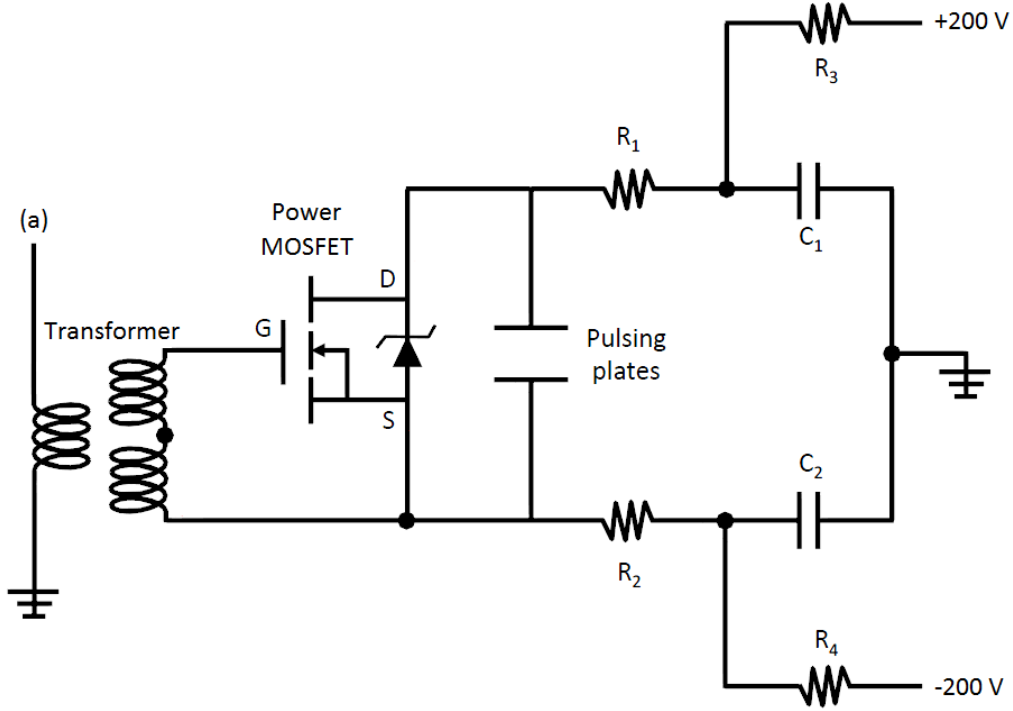


FIGURE 3.4. Pulsing circuit. $R_1 = R_2 = 470 \Omega$, $R_3 = R_4 = 20 \text{ k}\Omega$, $C_1 = C_2 = 680 \text{ nF}$. [30]

signals, which are recorded on a digital oscilloscope. An example of raw oscilloscope traces of Faraday cup 3 and induction plate signals are shown in Fig. 3.5(a). The pre-amp output voltage is related to the input current according to Eqn. 9:

$$(9) \quad I = \frac{-(V_{out} + R_1 C \frac{dV_{out}}{dt})}{R_1 M}$$

$R_1 C$ and $R_1 M$ are determined by putting a known square pulse into the pre-amp. First, the time constant of an exponential fit to the signal decay determines $R_1 C$, and then $R_1 M$ is determined by matching this shaped signal to the original square pulse. Actual currents in the induction plates and cup 3 are shown in Fig. 3.5(b). The induction signal is positive as ions are approaching the sensitive plate, and an equal but negative signal is seen after the

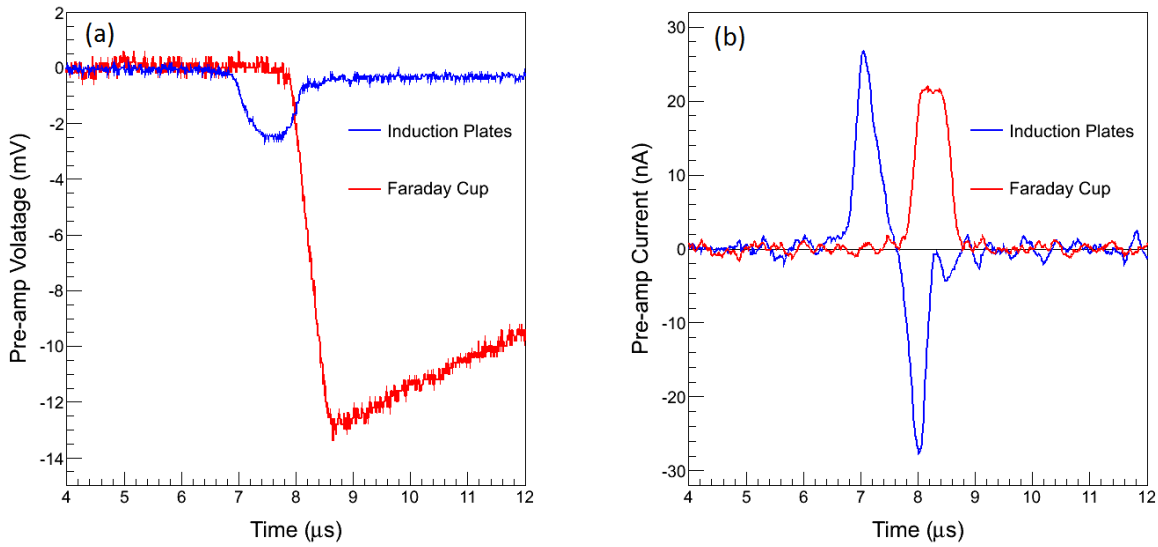


FIGURE 3.5. Raw (a) and shaped (b) pulse signals from induction plates and cup 3. The raw induction signal appears small because it is a less sensitive pre-amp (accounted for in shaping).

ions pass through. The Faraday cup stops the ions, so it produces only a positive induction signal as ions approach it.

Pulsing data also provides confirmation that the beam is composed of Ba^+ . The time between the center of the pulsing plate voltage overlap and the center of the pulse measured by the Faraday cup, along with a measurement of the distance traveled, provides a velocity measurement of the ions. This distance was measured to be 31.5 ± 0.5 cm from the center of the pulsing plates to the Faraday cup, and time-of-flight data, e.g. Fig. 3.6, give 39.8 ± 3.4 amu for Ar^+ and 136.8 ± 6.3 amu for Ba^+ , including an uncertainty on the time of flight of $\pm 0.1 \mu\text{s}$.

3.1.5. CALIBRATION OF ION DEPOSIT

To calibrate the signal at cup 3 to an ion density at the sapphire window, another Faraday cup (cup W) is attached to the cold finger in place of the sapphire window. The ratio of

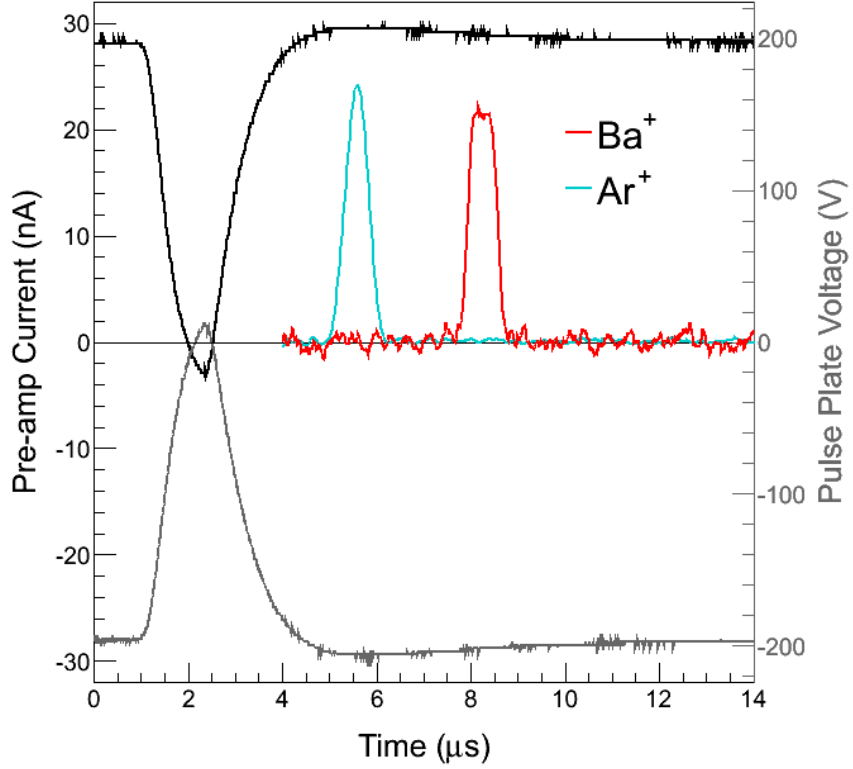


FIGURE 3.6. Arrival time of pulses at cup 3 vs. time of pulsing plate signal (black (+) and gray (-)) for Ar^+ and Ba^+ .

$\frac{fC}{pulse}$ between cup 3 and cup W is measured ($\equiv f$). Then, knowing the radius of the entrance aperture in cup W lets one determine the ion density per pulse at the sapphire window:

$$(10) \quad \frac{\text{ions}}{\text{pulse} \times m^2} = \frac{Qf}{eA}$$

where Q is the charge/pulse at cup 3, A is the area of cup W, and e is the elementary charge. The voltages on the final deflection plates H2 and V2 are also determined to optimize the signal in cup W. In later experiments, these differed from the values for maximum cup 3 signal by about 70 V in H2 and 60 V in V2, corresponding to about 4 mm in x and y position at cup W, indicating that some drift in optimal ion beam component settings occurred over time, either due to power supply drift or changes in the location of discharge in the source.

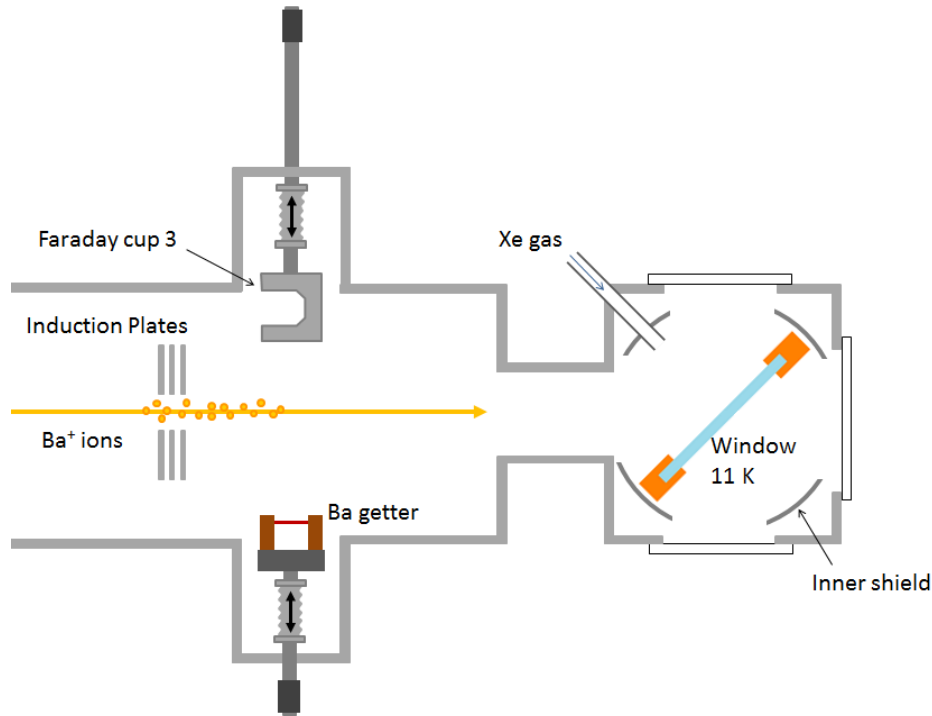


FIGURE 3.7. Apparatus near sapphire window, including Ba getter, Faraday cup 3, induction plates, and Xe gas inlet.

3.2. BA GETTER SOURCE

A BaAl₄ getter, manufactured by SAES, can be inserted on a bellows to emit toward the sapphire window, shown in Fig. 3.7. When heated, the getter emits neutral Ba with minimal Ba⁺. Getters were used extensively in previous work [31] for measuring the absorption of Ba in SXe with large Ba deposits, and in identifying emission peaks. A getter was used briefly in this work in identifying the 619-nm fluorescence peak, as described in Section 4.2. The barium getters used in [31] were exothermic BaAl₄-Ni flash getters. The getter used here is an endothermic BaAl₄ type, designed for more controlled Ba emission.

3.3. SAMPLE DEPOSITION

The Ba⁺/Ba is co-deposited with ultra-pure Xe gas onto a cold sapphire window. Sapphire has good thermal conductivity at low temperature and good optical transparency in

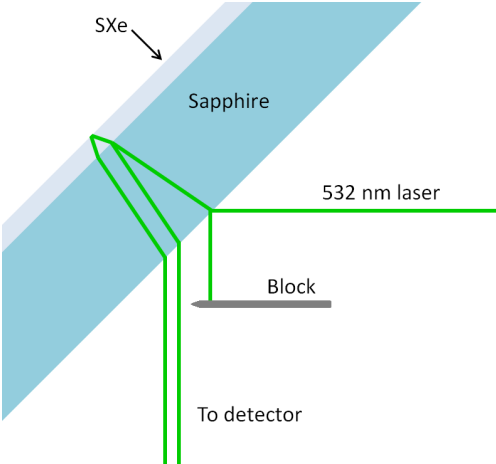


FIGURE 3.8. Setup for measuring SXe deposition rate by interference fringes.

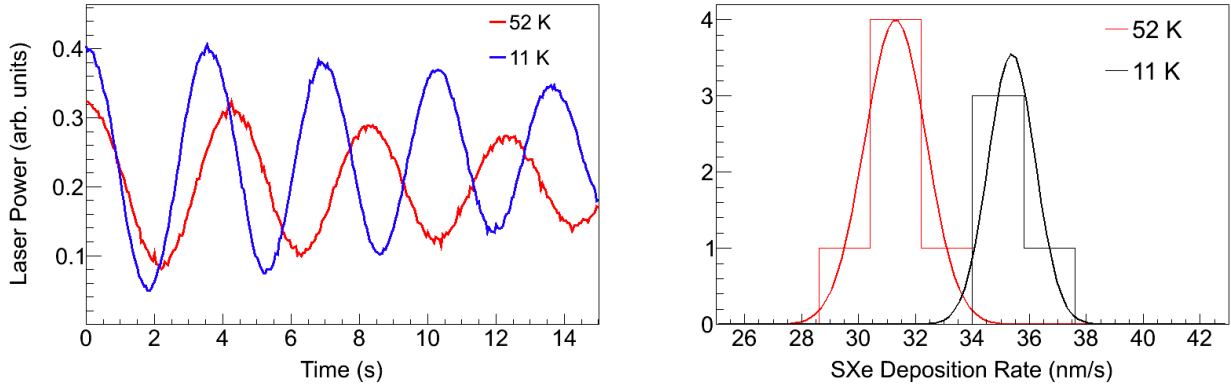


FIGURE 3.9. Interference fringes for the same Xe gas leak rate deposited on the sapphire window at 11 K and at 52 K.

the visible. The window is held in a copper mount attached to a coldfinger and is tilted at 45° to allow access of the ion beam and Xe gas, as well as the excitation laser and collection optics. To begin a deposit, Xe gas is flowed toward the window via a leak valve. Cup 3 is then retracted and the ion beam is pulsed, depositing Ba^+ ions into the SXe matrix as it grows. Cup 3 is then replaced, and the Xe leak stopped.

SXe matrix deposition rate can be measured by interference fringes in a laser reflected against the front surface of the sapphire window, as shown in Fig. 3.8. Fringes for SXe deposition at 52 K and 11 K are shown in Fig. 3.9(a) for the leak rate used in this work.

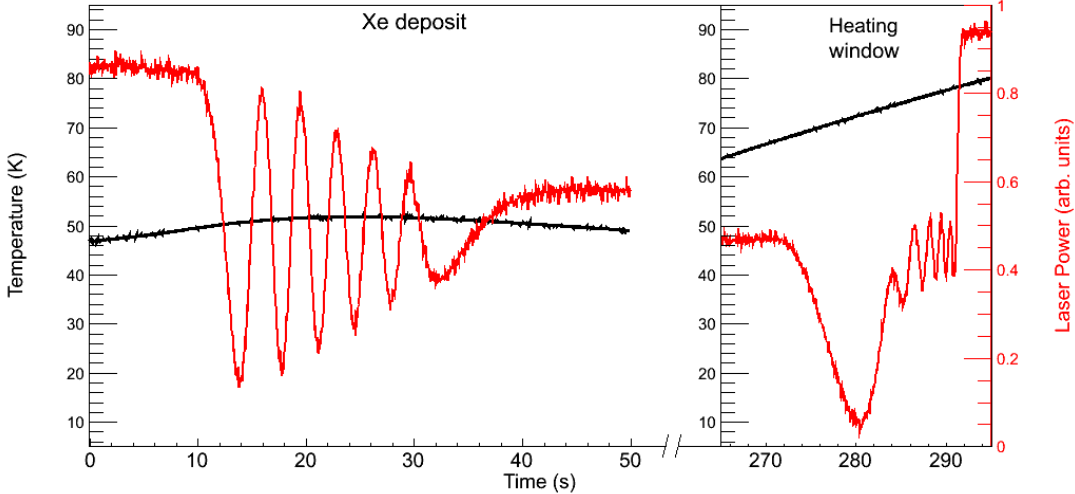


FIGURE 3.10. (a) Interference fringes of a deposit at 52 K and of its subsequent evaporation when heating the sapphire window, and (b) distribution of SXe deposition rates calculated from fringe period of several measurements.

The refractive index of SXe has a negligible dependence on temperature between 50 and 30 K [32], so these can be compared directly. A distribution of SXe deposition rate measurements from several deposits is shown in Fig. 3.9(b). A somewhat lower rate is observed at 52 K, $31.3 \pm 0.44(\text{stat}) \pm 0.31(\text{sys}) \text{ nm/s}$, vs. $35.4 \pm 0.41(\text{stat}) \pm 0.35(\text{sys}) \text{ nm/s}$ at 11 K. Statistical errors are σ/\sqrt{N} where σ is the standard deviation of the Gaussian fits to the distributions in Fig. 3.9(b), and N is the number of entries. Systematic errors come from propagating an uncertainty on the angle between the laser and sapphire window of $\pm 2^\circ$.

To evaporate a sample, the window is heated to 100 K. Fringes appear during this process as well. The full set of fringes for a deposit at 52 K and its evaporation when heated is shown in Fig. 3.10, along with the window temperature. This shows that the SXe evaporates between 73 K and 78 K. The same number of fringes appear in the deposit and the evaporation, indicating that the lower deposition rate at around 50 K is not due to simultaneous evaporation. The variance in temperature during the deposit is due to the

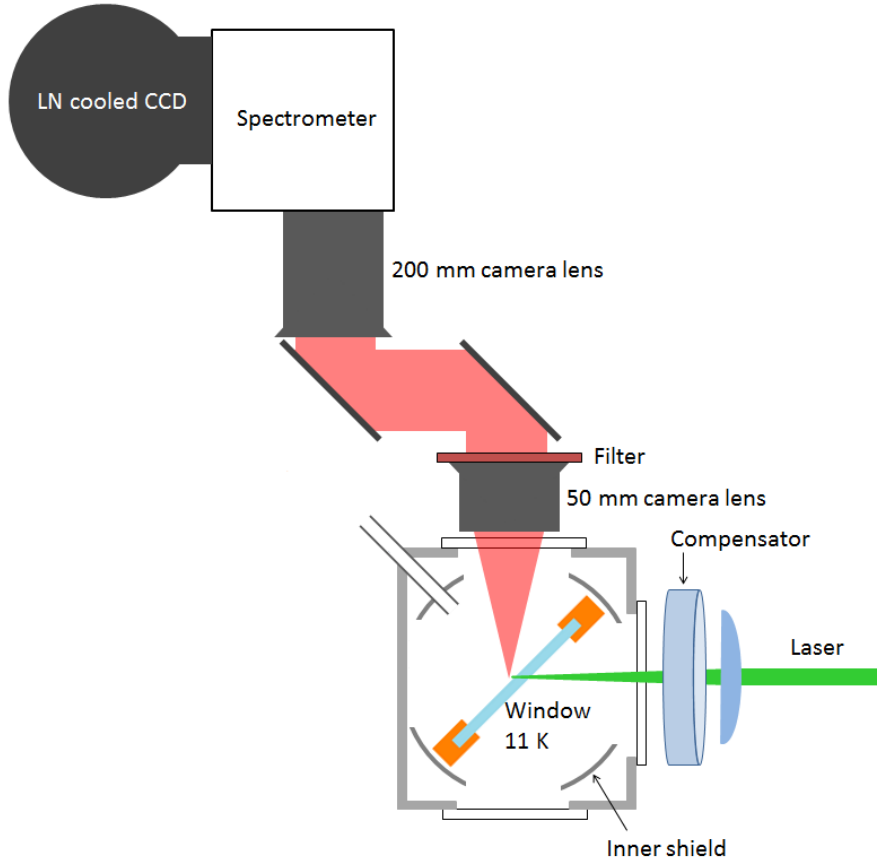


FIGURE 3.11. Apparatus in spectroscopy region, including optics for excitation, fluorescence collection, spectroscopy and detection.

heater cycle. Note that these Xe deposits were longer than for a typical deposit during a fluorescence experiment, in order to observe several fringes.

3.4. LASER EXCITATION

Green to yellow laser excitation was done with a Coherent 599 dye laser, pumped by the 514-nm line of a Lexel 3500 Ar ion laser. Rhodamine 110 (R110) dye was used for the 542 - 566 nm wavelength range, and Rhodamine 6G (R6G) for the 567 - 590 nm range. Another Coherent 599 dye laser with Coumarin 480 (C480) dye was used for blue excitation, which was pumped by a Kr ion laser. The Coherent 599 dye lasers were used with birefringent

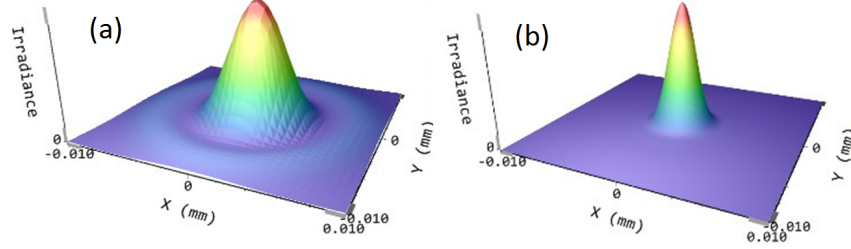


FIGURE 3.12. Calculated minimum laser spot size distributions, with wavelength 570 nm and unfocused waist $w = 7$ mm, for (a) bi-convex $f = 7$ cm lens, and (b) aspherical $f = 7.9$ cm lens.

filters for wavelength tuning, but without etalons, since the broad absorption of Ba in SXe does not require single-mode laser excitation.

A lens focused the laser into the cryostat from the side, shown in Fig. 3.11. Initial work, spectroscopy (Chapter 4) and some imaging, was done using a bi-convex, which produced spherical aberration near the laser focus. This effect does not affect the results in Chapter 4, where semi-focused beam waists of 100-1000 μm were used. However, spherical aberrations caused the minimum beam waist to be about twice that of the diffraction limit. To approach the diffraction limit in imaging small numbers (Chapter 5), a 7.9-cm focal length aspherical lens was used. A comparison of the minimum spot sizes for these two lenses, calculated by David Fairbank at Thorlabs, is shown in Fig. 3.12.

To correct for astigmatism introduced by the tilted sapphire window, compensating astigmatism was introduced by a fused silica optical flat of 1 cm thickness, placed after the lens, tilted on the y-axis (the laser is along the z-axis, and the sapphire window is tilted on the x-axis). The proper angle for the compensator was determined to be about 10° from normal by a ray matrix calculation [33]. The effect of the SXe layer is negligible since its thickness is only about half a micron in a typical fluorescence experiment. With the compensator, overlapping minimum spot sizes of $2.06 \mu\text{m}$ and $2.66 \mu\text{m}$ are calculated for x and y, respectively. To observe the astigmatism and the effect of the compensator, the relative position

of the x- and y-focus was observed by imaging 619-nm Ba fluorescence from a large deposit of Ba^+ in SXe, with a varying laser focus. For each z-position of the laser focusing lens, an image was taken, and a 2D Gaussian fit determined the x and y beam waists, w_x and w_y . Example fits to the 619-nm fluorescence for three laser focus positions, using the astigmatism compensator at $10 \pm 1^\circ$, are shown in Fig. 3.13(a,b,c). Gaussian fit values for w_x and w_y are plotted vs. laser focus position with (d) no compensator, and with the compensator at (e) $10 \pm 1^\circ$, (f) $13 \pm 1^\circ$, and (g) $11 \pm 1^\circ$. With no compensator (d), the focal positions for x and y are measured to be $127.6 \pm 2.5 \mu\text{m}$ apart. $10 \pm 1^\circ$ (e) and $13 \pm 1^\circ$ (f) can be seen to under- and over-shoot the optimal angle, respectively. $11 \pm 1^\circ$ (g), which was used in imaging experiments, is near optimal, i.e. the x and y foci are consistent to within $45 \mu\text{m}$. *A systematic uncertainty... on the beam size is then obtained ... leading to a focused laser spot of ?? \pm ?? μm^2*

3.5. COLLECTION OPTICS

Fluorescence was collected above the cryostat (Fig. 3.11). A 50 mm Nikon camera lens collimated the light, and a fluorescence filter sat on top of it. A band-pass filter was used for imaging, and a Raman filter was used for spectroscopy. The fluorescence then reflected off two steering mirrors, and was imaged by a 200 mm Nikon camera lens onto a Roper Scientific liquid-nitrogen-cooled CCD, with a magnification of 4. The CCD has a quantum efficiency of 90% in the visible, and in slow ADC mode, records one count per two photons collected. At the set point of -100 °C, dark counts are negligible.

The CCD has a removable Princeton Instruments imaging spectrometer. With this attached, the 200 mm camera lens focuses the light onto an inlet slit, which is then imaged by the spectrometer onto the CCD after reflecting off a diffraction grating. The 0-order

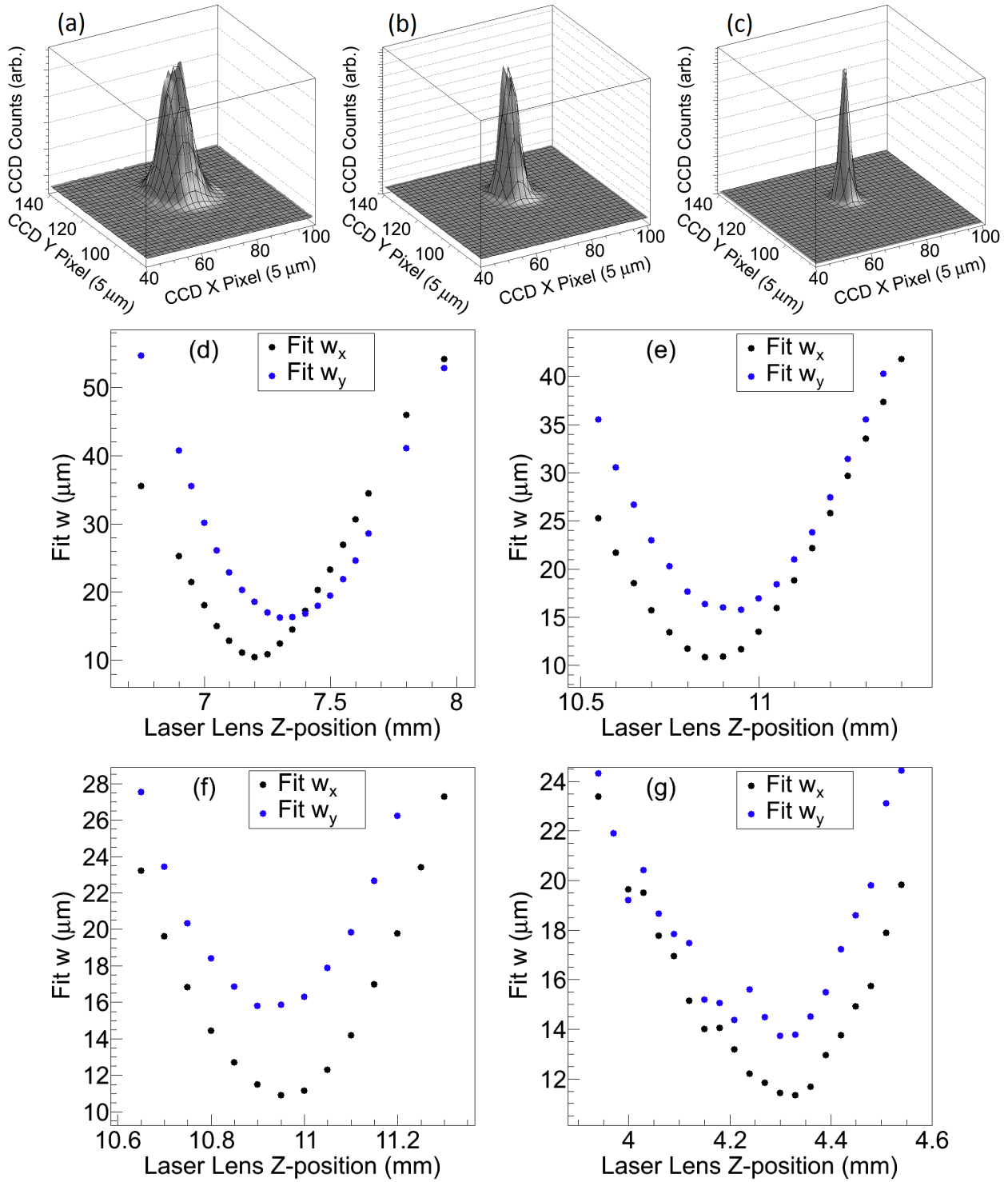


FIGURE 3.13. Example 2D Gaussian fits (black grid lines) with varying laser focus (a,b,c), and fit waists w_x (black) and w_y (blue) vs. laser focus lens position with (d) no compensator, and with compensator at about (e) 10° , (f) 13° , and (g) 11° .

reflection of the grating provides an image for alignment, and the grating can be tilted to distribute the 1st-order reflection across the horizontal CCD pixels for doing spectroscopy.

When a 1" diameter filter is used, the imaging system has a solid angle collection of about 1.5%. Each additional component in the collection optics, listed in Table 3.1, contributes some loss, resulting in a total collection efficiency (ϵ_c) of ?? with the spectrometer, and ?? without. The spectrometer also limits the system to an f-number of 4, though this is not limiting in this setup.

TABLE 3.1. Factors contributing to optical collection efficiency.

Component	Efficiency	
Cryostat Window	0.99	
Camera Lens 50 mm	0.89	
Camera Lens 200 mm	0.91	
Steering Mirrors ($\times 2$)	0.95	
CCD Quantum Efficiency	0.90	
Filter	0.98	
Counts per Photon (CCD)	0.5	$\epsilon_c(\text{w/o spectrom.}) = ??$
Spectrom. Mirrors ($\times 2$)	??	
Diffraction Grating	0.5	$\epsilon_c(\text{w/ spectrom.}) = ??$

To limit laser exposure to only the time of CCD exposure, a laser shutter was linked to the camera exposure with a LabVIEW program. This program also recorded laser power via a calibrated pickoff, as well as the temperature of the coldfinger near the sapphire window during observation.

3.6. VIBRATIONS AND EFFECTIVE LASER REGION

Relative vibrations between the laser and sapphire window affect the number of Ba atoms exposed, increasing the effective laser spot size. This was studied by observing the position of a “dust spot” (a highly scattering feature on the sapphire window) relative to the position of the laser in an image on time scales down to 50 ms. An example of an image from this

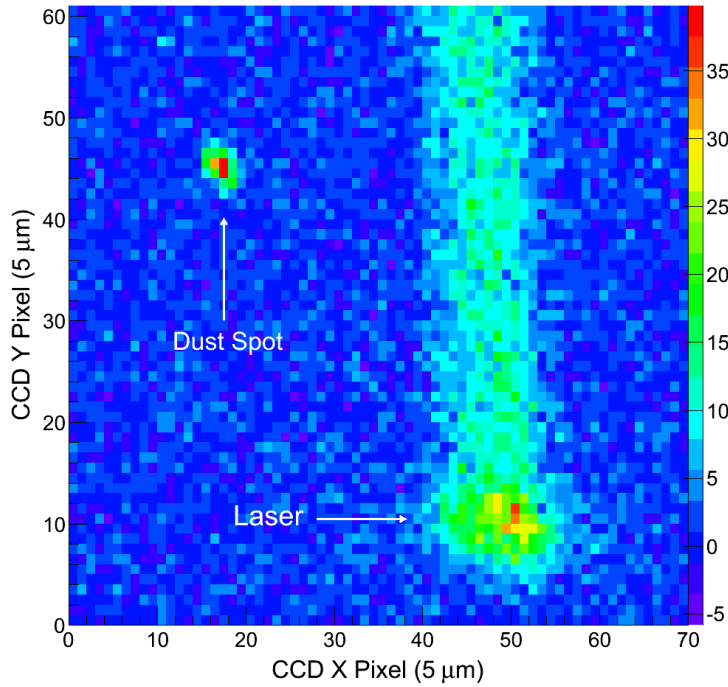


FIGURE 3.14. Example image of dust spot and laser during observation of cryostat vibrations.

experiment is shown in Fig. 3.14. The 570-nm dye laser was somewhat de-focused, and the dust spot was illuminated by a de-focused 657 nm diode laser. For each frame, 2D Gaussian functions were fit to locate the center of the laser spot and the dust spot in order to measure their relative position. The fit for the laser spot was restricted in y so that it was not affected by the bulk sapphire fluorescence path. The distances in x and y between the dust spot and laser are plotted for each 50-ms snapshot in Fig. 3.15(a). The distribution shows a correlation between x and y . To calculate an effective laser spot size due to this vibration, each difference (x,y) between laser and dust spot was used as the center of a 2D Gaussian, each with $w_x = 2.06 \mu\text{m}$ and $w_y = 2.66 \mu\text{m}$ to represent the laser spot. Such Gaussian functions were summed for all points to produce a distribution of summed laser exposure, shown in Fig. 3.15(b). The total area enclosed by a $1/e$ contour then represents the effective

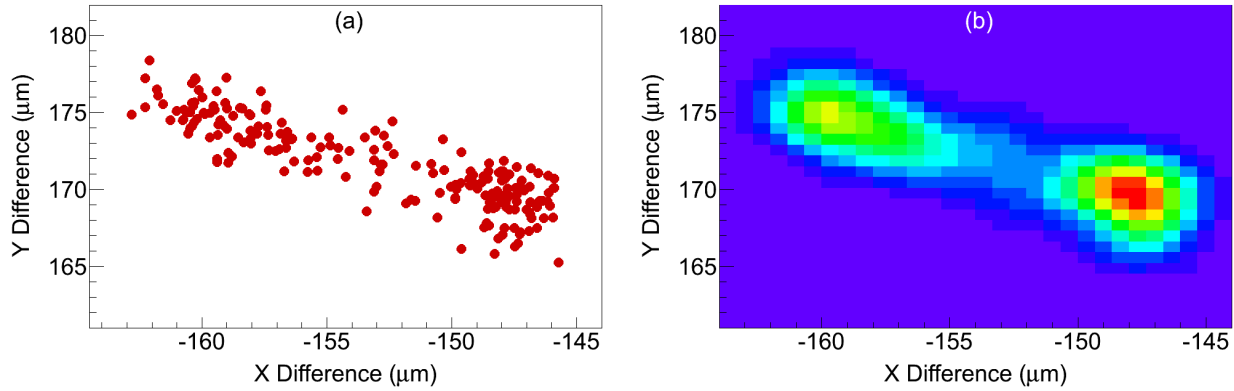


FIGURE 3.15. Cryostat vibration measurements based on relative position of dust spot vs. laser on sapphire window in 50-ms snapshots (a), with 2D Gaussians overlain on each point to represent total laser exposure vs. position (b).

area. Since x and y movement are correlated, and since the movement is sinusoidal, the effective area is only about $2 \times$ make an “if greater than or equal to $1/e$ ” thing for bins the real laser spot size, and the effective laser region is $17.8 \mu\text{m}^2$.

The aforementioned is the most concerning vibration to understand. Vibration of the laser itself is included in that study. Vibration of the collection optics will affect the imaging resolution, but not the number of atoms being observed. These vibrations were minimized by stable mounts.

3.7. LASER SCANNING

In order to obtain images of separated single atoms, the laser focusing lens is attached to motorized Newport translation stages which scan the laser position by scanning the lens in x and y, shown in Fig. 3.16. These stages sit atop a manual z-translation stage for laser focusing. An extension of the aforementioned LabVIEW program coordinates movement of these stages such that x or y position is stepped in between CCD frames, and each frame then corresponds to a position in a laser scan grid.



FIGURE 3.16. Asphere laser focusing lens mounted to motorized Newport translation stages for laser scanning.

Show data on steps and reproducibility – say this isn't good and new stages will be used later.

CHAPTER 4

RESULTS: SPECTROSCOPY

The spectroscopy of Ba in SXe was studied in detail beyond that reported in [30, 31], with the goal of imaging single Ba atoms. Emission and excitation spectra are analyzed in 4.1, with particular interest in the origin of the 619-nm peak in 4.2. Studies of temperature and bleaching effects in 4.3 and 4.4 aid in determining optimal conditions for observation. Backgrounds are analyzed in 4.5 in order to optimize sensitivity, and finally, candidate emission lines for Ba^+ in SXe are discussed in 4.6.

4.1. EMISSION AND EXCITATION OF BA IN SXE

Deposits of Ba in SXe absorb primarily between 540 nm and 570 nm. An absorption spectrum, obtained by observing absorption of white light by a large Ba deposit at 11 K, is shown in Fig. 4.1, along with an example emission spectrum of a Ba^+ deposit made at 45 K and observed at 11 K with 557 nm excitation. Significant broadening, as well as a 4-nm redshift of the central peak, occur relative to the vacuum $6s^2 \ ^1\text{S}_0 \rightarrow 6s6p \ ^1\text{P}_1$ absorption value of 553.5 nm. Initial discovery of this absorption and emission was done with the purely neutral Ba getter source. Observation of the same spectra from Ba^+ ion beam deposits demonstrates some neutralization of the ions. The fraction of ions neutralized is not determined. [19, 30, 31]

The several red-shifted emission peaks observed are attributed to Ba atoms occupying different matrix sites in the SXe. Deposition at temperatures higher than 11 K and exploration of more excitation wavelengths have led to discovery of a few emission peaks beyond the 591- and 577-nm peaks reported in [30] and [31]. Emission spectra for selected excitation

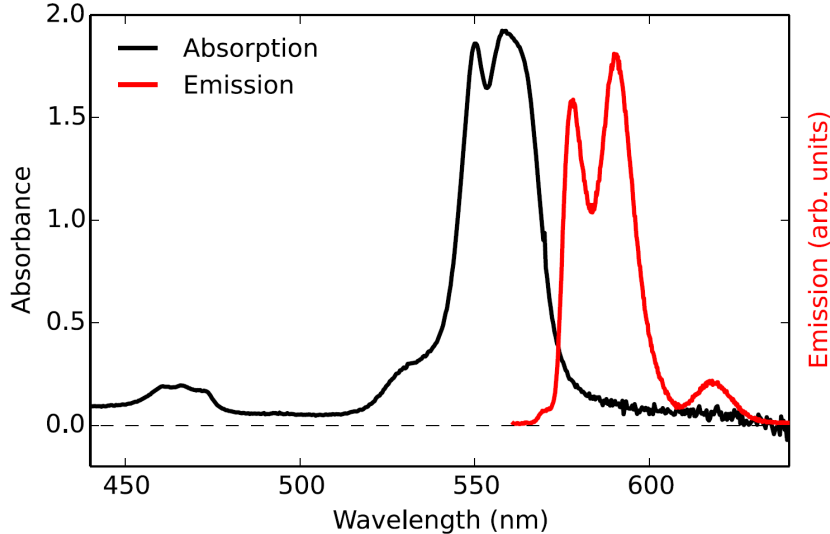


FIGURE 4.1. Absorption and emission spectra of neutral Ba in SXe. The absorption is of a Ba getter deposit at 10 K, and the emission is of a (neutralized) Ba^+ deposit, deposited at 45 K and observed at 11 K with 557 nm excitation.[19]

wavelengths are shown in Fig. 4.2(a), for a deposit made at 44 K and observed at 11 K. These selections are part of a full excitation spectrum, shown in Fig. 4.2(c). An excitation spectrum is produced by scanning the dye laser and measuring the magnitude of each fluorescence peak vs. excitation wavelength. For each 1-s CCD exposure, a sum of *don't call them this* asymmetric Gaussian functions and standard Gaussian functions is fit to the spectrum after pedestal subtraction. The asymmetric Gaussian fit function used, which fits the 577- and 591-nm peaks somewhat better than standard Gaussians, is $A(1+\text{erf}(\frac{x-a}{\sigma_1})(1-\text{erf}(\frac{x-a}{\sigma_2}))$, where A is the free amplitude parameter. The peak position a is fixed for each peak, as are the left and right smearing widths σ_1 and σ_2 . The function $\text{erf}()$ is a Gaussian error function. The asymmetric Gaussian function is not perfect for all frames, as the shape of the emission can depend on the excitation wavelength. An example frame with fits is shown in Fig. 4.2(b). The full fit is the dotted black line, and each peak's contribution is in color. Curves in (a) have about $100\times$ the laser power used in the excitation spectrum (e.g. (b))

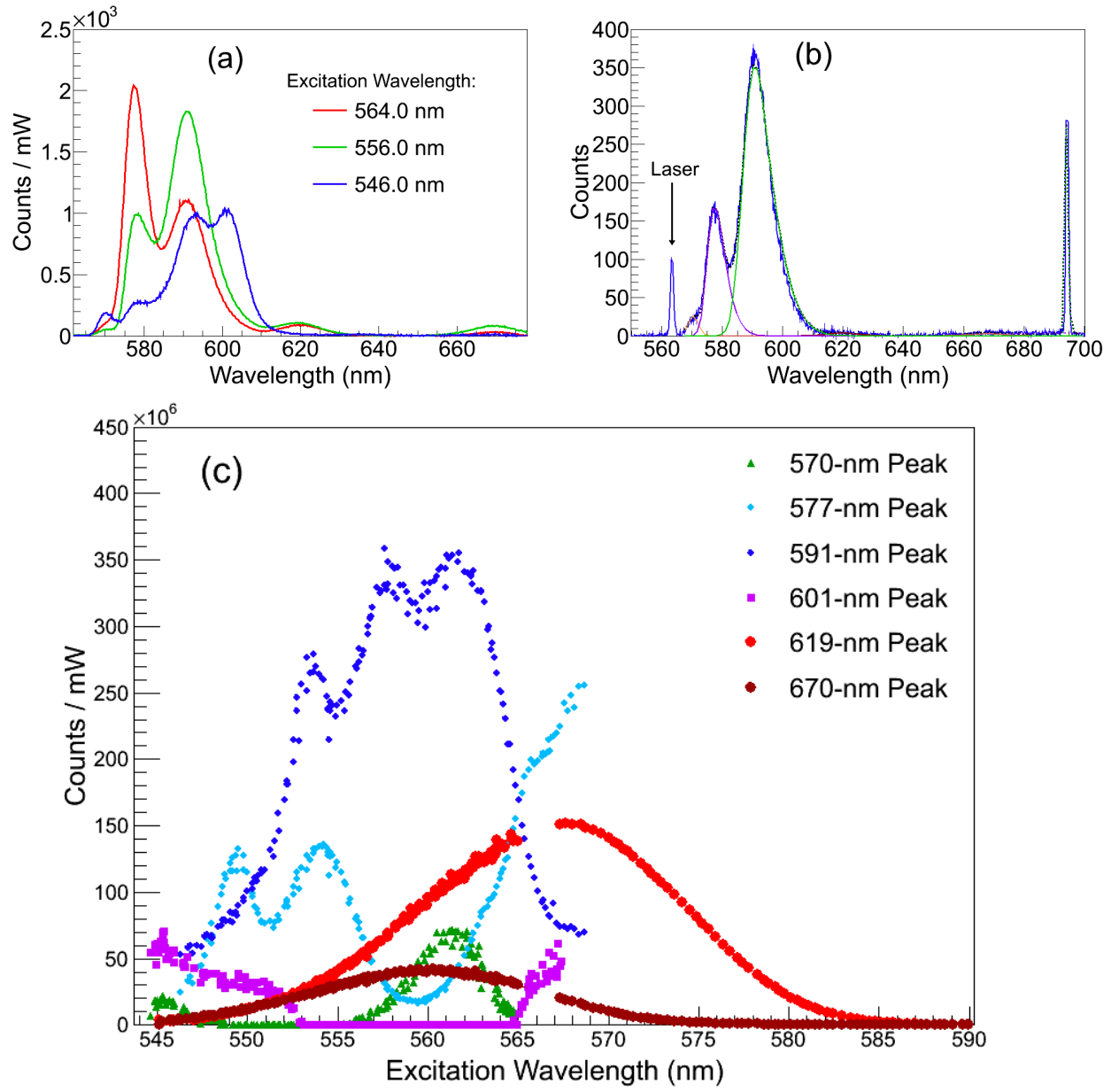


FIGURE 4.2. Background-subtracted fluorescence spectra for a few different excitation wavelengths (a), an example fit to a spectrum (b), and full excitation spectra for all observed Ba fluorescence peaks (c). Magnitudes in (c) have been scaled for visibility on the same plot (relative magnitudes are arbitrary as they are affected by relative site populations and fluorescence efficiencies). The discontinuity around 566 nm for the 619- and 670-nm peaks is the boundary between usage of different laser dyes. R6G dye is used for higher wavelengths and R110 for lower wavelengths and for all other curves. Curves for the R6G segments (619- and 670-nm peaks) require special scaling to line up with their respective R110 segments, and this scaling was different between the 619- and 670-nm peaks, likely due to different relative populations of those sites on the different deposits.

where low intensity is desired to avoid bleaching during the scan. Rather than attempting frame-by-frame background subtractions, additional Gaussians are fit to the broad and sharp background fluorescence. These backgrounds and their excitation spectra are discussed in 4.5. A 566 nm Raman filter was used to attenuate the majority of the laser scatter, however the small amount of scatter passed by the filter was used to determine the frame's excitation wavelength. Each peak's fit contribution was then integrated and scaled by the frame's laser power, as the power output is not constant through the dye range.

Wavelength calibration was done using three lasers whose wavelengths were first measured with a Burleigh Wavemeter: a red diode laser at 656.99 nm, a doubled Nd:YAG laser at 532.23 nm, and the C480 blue dye laser typically around 475 nm (at 488.91 nm for the data in Fig. 4.2). These lasers were directed at the same position on the sapphire window, and their scatter was imaged along the same path as the Ba fluorescence. The WinSpec software applies the diffraction grating equation to calibrate each CCD pixel to a wavelength.

4.2. 619-NM PEAK IDENTIFICATION

The 619-nm peak, as well as the 670-nm peak, was attributed to neutral Ba by a few further tests. A large Ba⁺ deposit is compared to a deposit made with the Ba getter in Fig. 4.3(a). The 619-nm and 670-nm peaks were observed with both sources, and since the getter produces only neutral Ba, they were attributed to neutralized ions in Ba⁺ deposits. Observation of the fluorescence with two different types of Ba sources is itself positive. In addition, observation of the fluorescence with the low deposit energy of the getter may bode well for the prospect of grabbing on a probe in LXe. Observation of a large deposit of Ar⁺ in SXe is also shown in Fig. 4.3(a). The lack of fluorescence further disfavors a matrix-damage-related source of the fluorescence, such as color centers. Finally, to rule out the

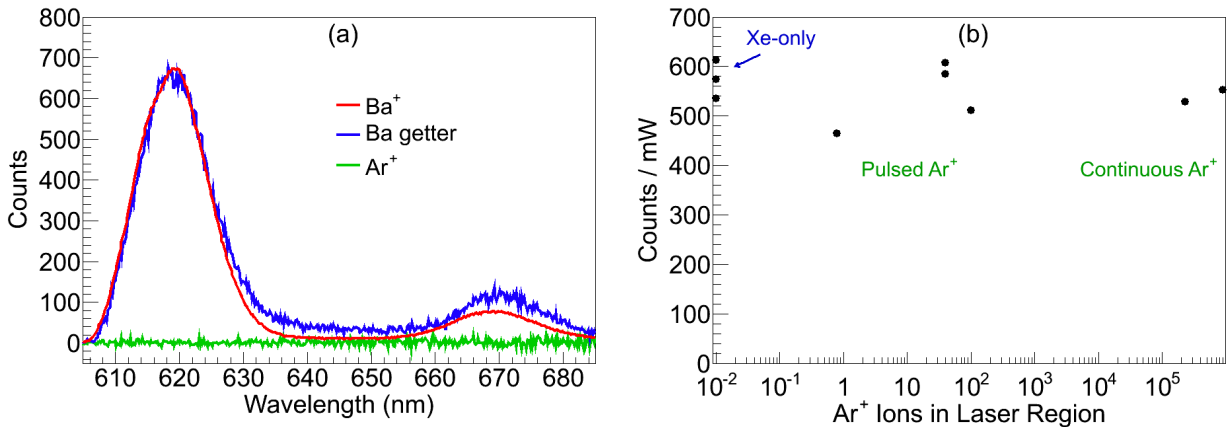


FIGURE 4.3. Comparison of signal observed for deposits with the Ba^+ ion beam (red), Ba getter (blue), and Ar^+ ion beam (green) (a), and signal through 620-nm band-pass from deposits of small to large numbers of Ar^+ ions in SXe.

possibility that the signal in Ba imaging experiments is due to passed wavelengths far from the 620-nm band-pass region, e.g. infrared, imaging experiments of Ar^+ deposits in SXe were performed with both pulsing and continuous ion beams. The same 620-nm band-pass filter was used, as well as the same focused 570-nm laser, to be similar to Ba^+ 619-nm imaging experiments. Summed counts from these deposits were consistent with background, as shown in Fig. 4.3(b).

4.3. ANNEALING/TEMPERATURE DEPENDENCE

Matrix site occupancies for Ba atoms can depend on annealing history, and similarly on the temperature at which a deposit is made. Spectra under different temperature conditions are shown in Fig. 4.4. Peak shapes look similar for deposits made at 40-55 K as those made at 11 K and then annealed to 40-55 K, both being observed at 11 K, though relative amplitudes are not the same, likely due to matrix site populations. Without annealing, 11-K deposits have a different peak shape around 590 nm, with a broader peak centered around 596 nm. It is possible that the broader shape is due to a higher population of the 601-nm

peak, and it is not resolved from the 591-nm peak. The experiment in Fig. 4.4 did not have optimal laser intensity for observing behavior of the 619-nm peak; a study of deposit conditions for this peak is shown in Fig. 4.5. In that experiment, the 619-nm fluorescence was observed in a focused laser beam at 570 nm, in an image through the 620-nm band-pass filter. About $3\times$ more 619-nm fluorescence was observed in the deposit at 52 K vs. 11 K for the same leak rate (the respective 31 nm/s and 37 nm/s are from the same Xe leak rate, resulting in different SXe deposition rates according to Fig. 3.9). Also in this figure is a deposit at 11 K with the lower leak rate resulting in about 5 nm/s SXe deposition, which produced nearly $3\times$ lower signal than the leak rate resulting in 37 nm/s SXe deposition. Using the 10 K SXe density of 3.780 g/cm³ [34] and a typical Ba⁺ ion current density of 1.6 nA/mm² at the sapphire window, 5 nm/s and 37 nm/s correspond to Xe:Ba ratios of about 8.7×10^3 and 6.4×10^4 respectively. Xe leak rates above 37 nm/s result in rapid frosting of the SXe matrix, which causes blurring of the image and high laser scatter. These tests guided the standard of depositing with Xe leak rate resulting in 31 nm/s SXe deposition at 50 ± 5 K when observing the 577-, 591-, and/or 619-nm peaks. The different bleaching behavior in the low Xe leak rate deposit is interesting but not well understood.

Fluorescence spectra with 564 nm excitation through several annealing cycles for a deposit made at 11 K are shown in Fig. 4.6. At this wavelength, all observed Ba peaks are prominent except the 570-nm peak. Similar to excitation spectra, individual fluorescence peak amplitudes can be plotted vs. temperature by fitting the full spectrum in each frame. Rather than asymmetric Gaussians, this analysis used standard Gaussian and Lorentzian functions. Lorentzians fit the 619-nm and 670-nm peaks well. Each individual peak's amplitude is plotted vs. temperature in Fig. 4.7(b-f), with an example of a fit spectrum in Fig.

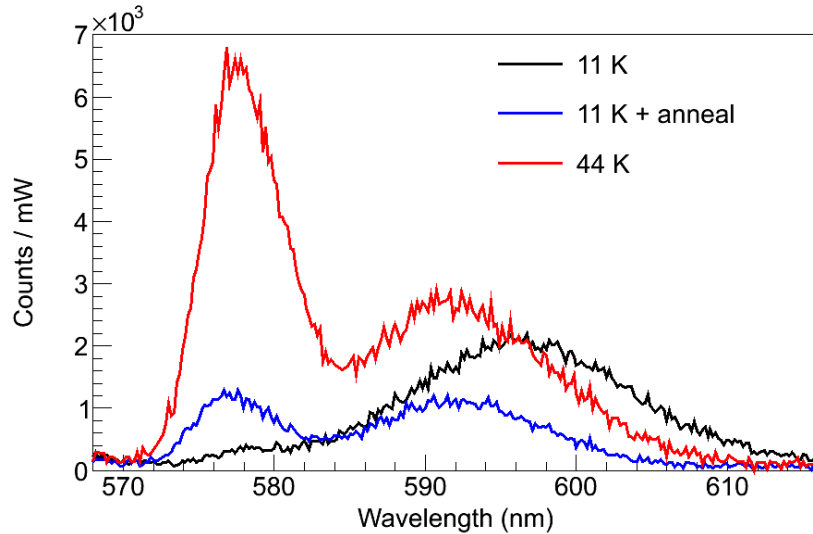


FIGURE 4.4. Spectra of peaks around 590 nm of a Ba^+ deposit made at 11 K before and after annealing to 39.4 K, and one made at 44 K. All observations are at 11 K. Both Ba^+ deposits are 15 s, however the 44 K deposit is scaled slightly to account for different ion current. Laser power was about 0.1 mW with an unfocused beam waist of $w = 7.056$ mm, at 566 nm wavelength.

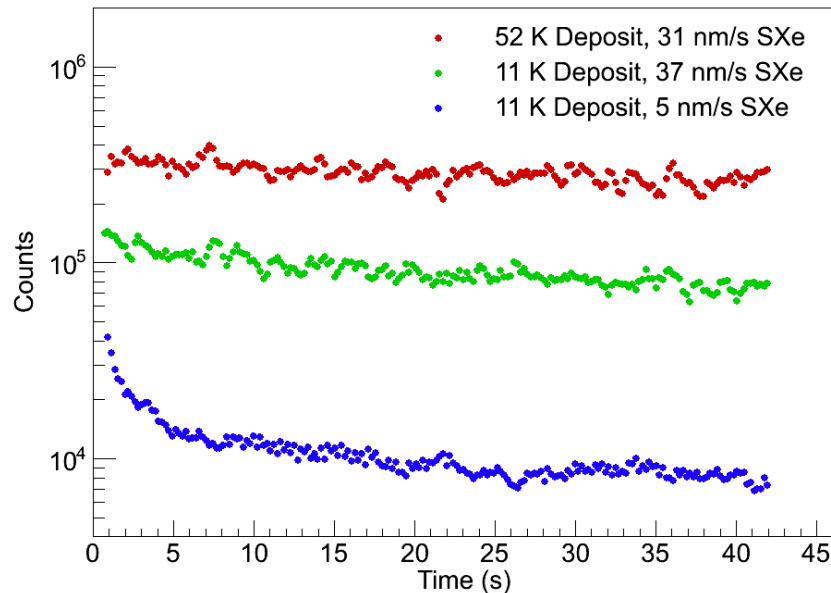


FIGURE 4.5. I guess just do custom-binned single points to show initial signal level for each type 619-nm fluorescence counts over time from imaging focused 570-nm laser region, for Ba^+ deposits at different temperature and Xe leak conditions. Frame times are 0.1 s, with time in between frames of about 0.11 s.

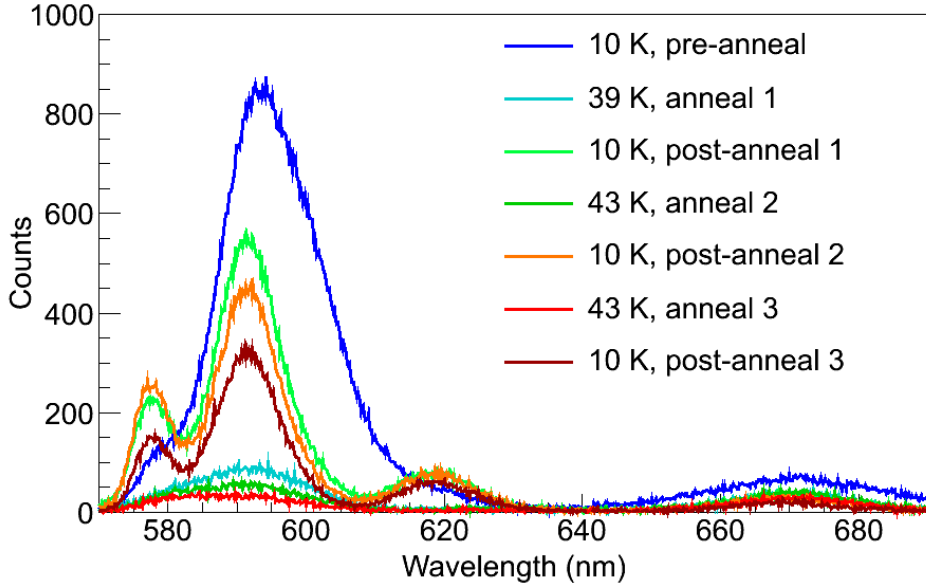


FIGURE 4.6. Spectra of a large Ba^+ deposit through several annealing cycles. Initial deposit was at 11 K. Laser power was about 0.2 mW with an unfocused beam waist of $w = 7.056$ mm, at 564 nm wavelength. These are selections from the full data set shown as peak counts vs. temperature in Fig. 4.7. [19]

4.7(a). In this interpretation, the 601-nm peak along with the 591-nm peak fit the broader peak in the initial 11 K deposit. The 601-nm peak had nearly complete loss in the first anneal cycle. The 670-nm peak had significant loss, with more loss after each succeeding anneal cycle, each of which reached higher a temperature than the last. The 591-nm had moderate loss with each cycle. The 577-nm and 619-nm peaks gained significantly with the first anneal, suggesting that they are due to more stable matrix sites. Both peaks remained about the same after the second cycle (small gain in 577-nm), and both had loss after the third cycle, which reached the higher temperature of 48 K. This could be due to greater diffusion at higher temperature leading to Ba/Ba interactions.

Aside from matrix site changes, direct temperature dependence of fluorescence can be observed in annealing cycles. The 577-, 591- and 619-nm peaks have their highest amplitude at 11 K. The 577-nm and 619-nm peaks appear to be leveled off at 11 K, while the 591-nm

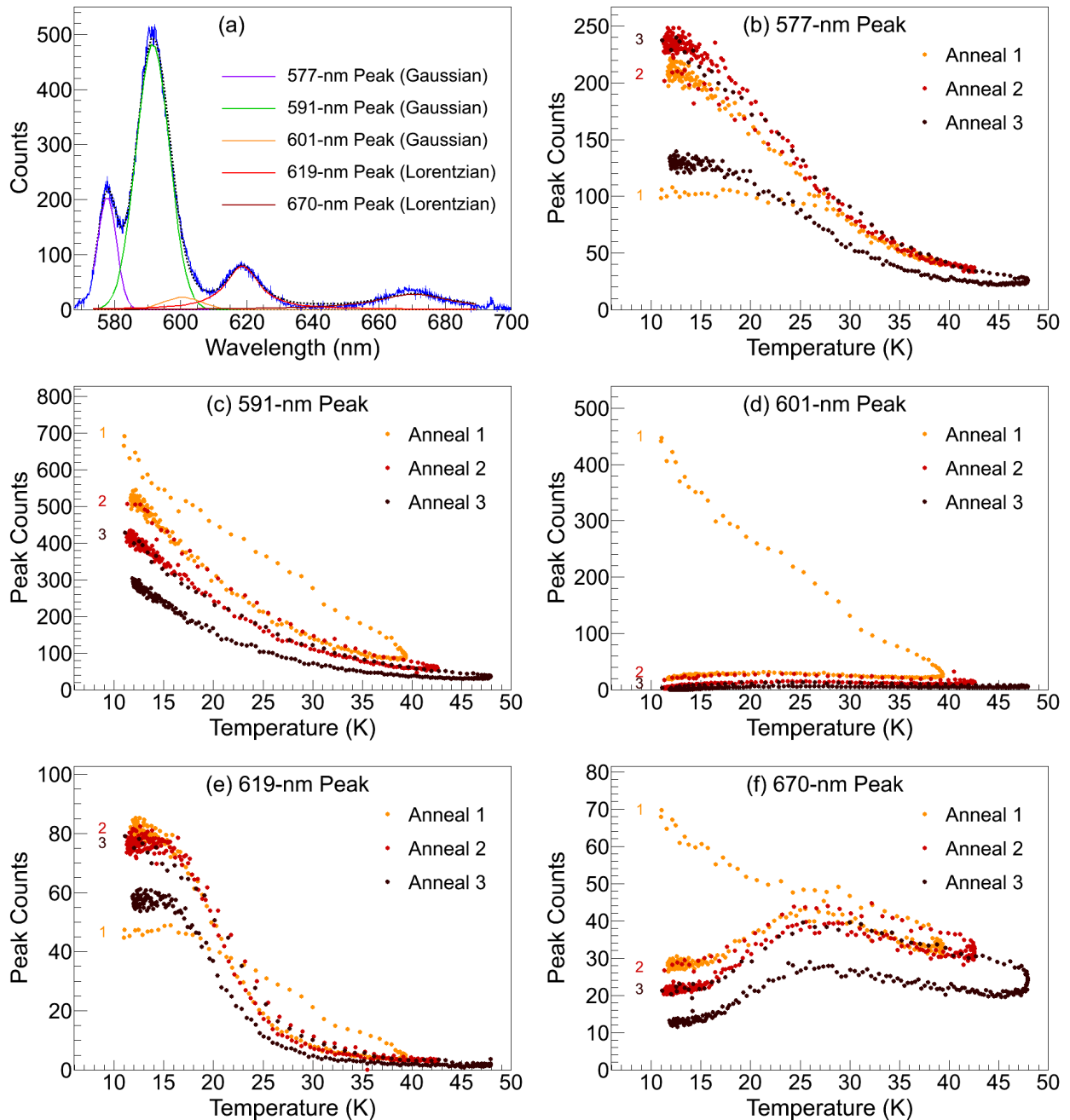


FIGURE 4.7. Example fit with standard Gaussians and Lorentzians (a) and fit peak counts for each fluorescence peak through three annealing cycles of the Ba^+ deposit made at 11 K (b-f). “1, 2, and 3” mark the beginning of each anneal cycle. Laser power was about 0.2 mW with an unfocused beam waist of $w = 7.056$ mm, at 564 nm wavelength.

may benefit from even lower temperatures. The 670-nm peak has its highest amplitude at around 25 K (apparent after its major site alteration has occurred). This inverse relationship

between fluorescence and temperature suggests that a probe in nEXO will need to be moved to an evacuated chamber in order to cool to 11 K or below for observation.

4.4. BLEACHING

Just show bleaching, as informant on how to image, rather than showing model fits.

Decay of fluorescence with laser exposure, or bleaching, was observed for all six Ba fluorescence peaks. It is a rapid process for the 570-, 577-, 591-, and 601-nm peaks, and a much slower process for the 619- and 670-nm peaks. With the prospect of counteracting the effect for single-atom imaging, bleaching of the 577- and 591-nm peaks was studied in detail by observing the fluorescence decay rate for varying excitation rates.

To produce a well-known laser intensity, the laser was de-focused to a specific beam waist (w), and the image of 619-nm fluorescence (which defines the laser region due to its low bleaching) from a large Ba^+ deposit was centered in the spectrometer slit and a y-pixel region of interest (ROI) with edges at 90% of the maximal intensity. Ba spectra over time are shown in Fig. 4.8(a,b,c) for excitation at (a) 556.9 nm, (b) 562.6 nm, and (c) 566.3 nm, where relative bleaching rates between peaks can be seen to depend on the excitation wavelength. Fluorescence counts vs. total excitations (excitation rate $w_{12} \times \text{time}$) for the 570-, 577-, and 591-nm peaks are plotted in Fig. [fig bleaching]. ...I swear this doesn't make sense, because you KNOW $1/x \times t$ and $x \times I$ does not yield the same total counts...maybe you just want to globalize ones with the same I and t , or just compare differently don't forget the correction on p-meter sensitive area and on p-meter quantum efficiency Note that the 577-nm peak has a lower bleaching rate when excited in the region around 566 nm. This informed the usage of x nm in imaging this fluorescence in 5.1.

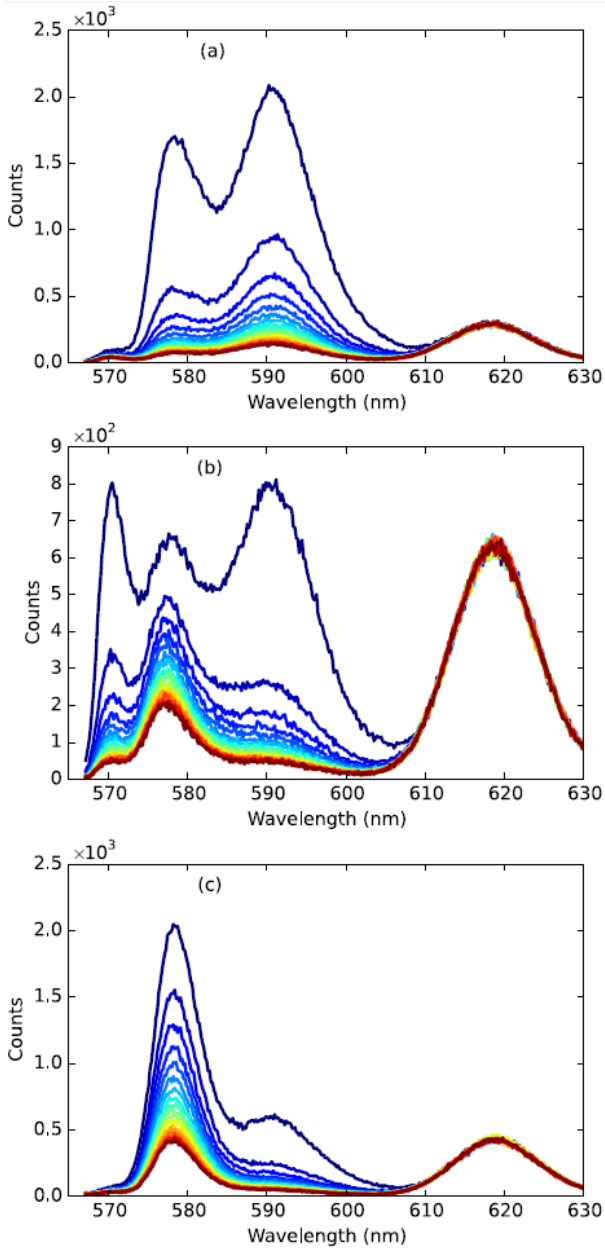


FIGURE 4.8. will re-do these, ideally showing 670-nm. [19]

The 6-level model solved in [sec. in Ch. 2] can be applied to this bleaching data to determine deviations from vacuum transition rates. The 6th level allows for one additional vacuum-forbidden transition from the excited state, a_{26} and its decay back to ground a_{61} , e.g. a 3P state. A successful model will fit observed bleaching curves for all values of w_{12} with the same transition lifetimes. An example *examples of* of a good model fits is shown in Fig.

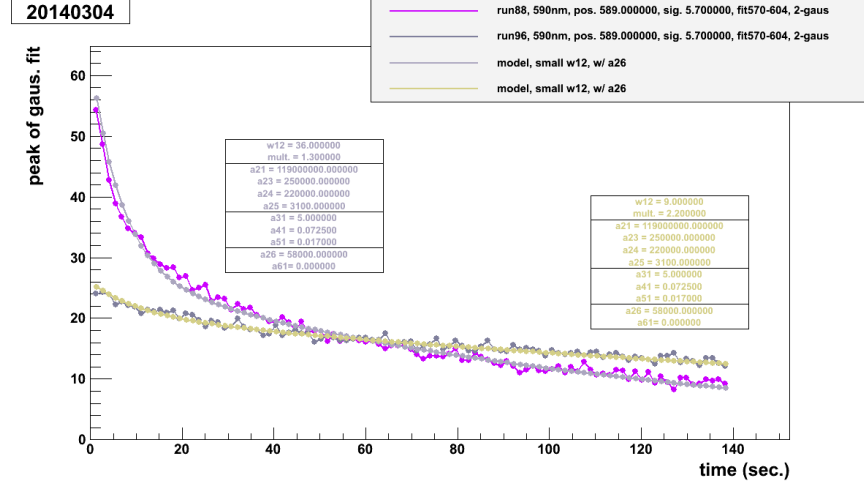


FIGURE 4.9. example place-holder

4.9. The nearly constant decay slope in later frames was easily fit with the introduction of non-zero a_{26} , and could not be fit by manipulation of the existing transitions, suggesting the presence of an additional matrix-induced path out of the excited state. In addition, non-zero a_{61} values only hurt the fit, suggesting that this state does not have a spontaneous recovery path (*is this just for one of the peaks?*). An important observation is that the other rates do not require much change from their respective vacuum values, with the exception of *whatever that one is. try non-changed $a_{2?}$, to see if maybe the extra .5-s is actually in between each frame ... go into the lab and try come where this ,5-s would dominate and see if it's there* This suggests that the observed bleaching is mostly due to optical pumping into the metastable D states, with the exception of a_{26} , and thus that laser re-pumping should be possible to increase the fluorescence signal from these peaks.

Another interesting result is the model's inability to explain the low fluorescence efficiency (ϵ_f) observed in these peaks. The number of counts observed is significantly lower than expected from $a_{21} = ?$. ϵ_f , defined in [Ch.2], was measured by the total counts observed in the first frame of exposure divided by its respective w_{12} , shown in Fig. 4.10. This method of

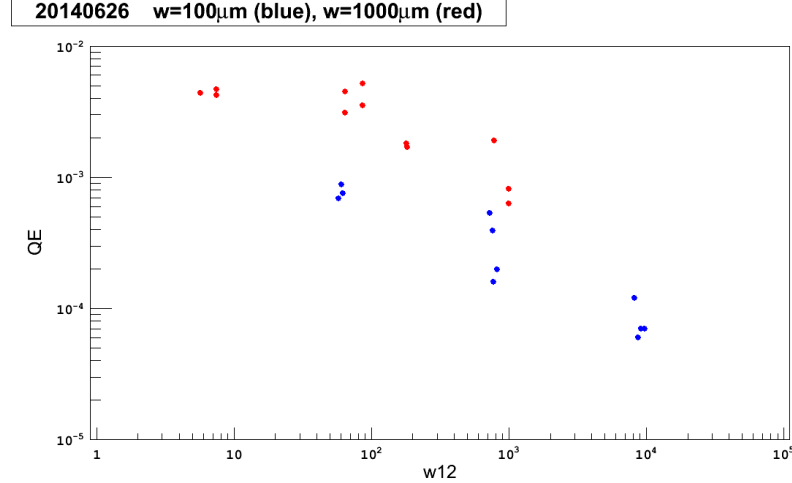


FIGURE 4.10. *correct this too for real w_{12} , and needs some correction to combine the two regions?*

measuring ϵ_f becomes less accurate with more optical pumping in the first frame, i.e. with higher w_{12} for a given frame time. Thus, the trend should be extrapolated toward zero. Since it seems to be leveling off in the lowest w_{12} values, the trend suggests a real ϵ_f of about **0.5%**. The bleaching model was unable to explain this low ϵ_f by additional paths out of the excited state without introducing extreme alterations to existing rates, or by introducing extreme a_{26} and a_{61} , in order to dominate a_{21} . A possibility is that the low count rate actually reflects a matrix site population by only about 1% of deposited Ba⁺ ions. *I bet $w = 100 \mu\text{m}$ is more likely to be the wrong one ... does that one require that more extreme w_{12} change in modeling (or, the one that still requires a fix after the right P correction has been applied)?*

Effective re-pumping of optically pumped Ba could require up to three additional lasers, one for each of the populated metastable D states, as it does in vacuum. The optimal absorption for each transition would need to be discovered using tunable lasers in the infrared, and the search would be challenging, as the effect of re-pump is small until all three are achieved. However, mixing of states in the Xe matrix could lower the number of lasers needed. Searches for an effect of additional excitation lasers were attempted with a few

different lasers. A 1550-nm diode laser and a 1064-nm Nd:YAG laser were used to attempt re-pumping from the ^1D and ^3D states, respectively. A 657-nm diode laser was used to attempt excitation from the ^3D states into the higher-level $5d6p\ ^3\text{D}_1$ state, which in vacuum has a path back to ground, as utilized in the Ba MOT in [24] for the $6d5d\ ^3\text{D}_1$ state with 659.7 nm. The blue C480 dye laser and 406-nm Kr ion laser were used to attempt excitation from the ^1D state into the higher-level states $6s7p\ ^1\text{P}_1$ and $6s8p\ ^1\text{P}_1$, respectively, which have paths back to ground in vacuum.

The only effects observed on bleaching rates by these re-pump lasers were increased bleaching by the blue dye and 406-nm Kr ion lasers. Some effect of a return of fluorescence was observed after separate exposures of low-intensity 406-nm Kr ion laser, shown in Fig. [fig Kr return]. In this experiment, bleaching of the 591-nm peak was observed by x-nm excitation, and then the x-nm laser was blocked for a length of time, either for a waiting period or for exposure to the 406-nm laser. Larger returns in 591-nm fluorescence were observed with 406-nm exposure than for periods of just waiting, for low intensities of the 406 nm. However, co-exposure of this intensity of 406 nm with the green excitation laser had no noticeable effect. This phenomenon was not explored further.

The 619-nm peak bleaches at much higher laser intensities. At a few mW of around 570 nm, bleaching is observed when the laser is focused. Integrated 619-nm fluorescence, divided by laser power, vs. time from an image of a focused 570-nm laser is shown in Fig. 4.11 for three laser powers. Observation of lower total counts when laser intensity and exposure time are increased and decreased, respectively, by the same factor, i.e. the same number of photons on faster time scales, indicates a time-dependent return mechanism for the fluorescence. This could be a return from a metastable state. Alternatively, if the

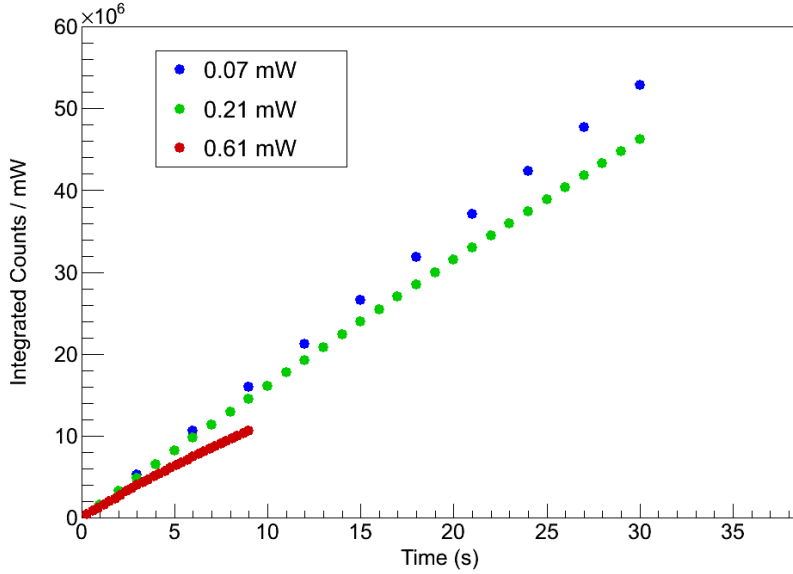


FIGURE 4.11

619-nm bleaching is caused by laser-heating of the sample (likely by heating the sapphire window), then the time-dependent return could be defined by the cryostat cooling power. Faster exposure times are more convenient, however this must be balanced against a loss of signal-to-noise. The 0.21 mW laser power was chosen, corresponding to an intensity of about $11.8 \mu\text{W}/\mu\text{m}^2$.

4.5. BACKGROUNDS

Should show the S/\sqrt{B} , and perhaps do a new one with the surf-bg-dominated spectrum to say maybe x should be used instead, but maybe not.

One source of background emission was observed from the surfaces of the window. Its broad fluorescence is shown in Fig. 4.12(a) with a 610-nm Raman filter cutoff and 570.4 nm excitation, and its excitation spectrum is shown in Fig. 4.12(b) over the R6G dye range. The nature of this emission has not been determined, however a few features were identified. One was that the emission increased as the window temperature was decreased, down to about 100 K where it remained flat down to 11 K, shown in Fig. 4.13. Another feature of the surface

background is that it bleaches with laser exposure. This was useful in that the background could be reduced by pre-bleaching of the window. However, the bleaching behavior also presented an inconvenient time dependence of the surface background, as historical bleaching and possible slight movements of the laser could lead to variation. Frequent Xe-only deposits were made in order to establish proper background subtraction. Spacial variation in the background is especially cumbersome in a laser scanning experiment, as discussed in 5.3. Given these behaviors, it is possible that the surface background is caused by a species which freezes to the window, or something which coats the window and fluoresces more at lower temperatures. In either case, the bleaching could be explained by evaporation with laser heating, or by optical pumping of the species into a metastable state.

Another source of background is fluorescence from the sapphire window. A spectrum of this fluorescence with 562 nm excitation is shown in Fig. 4.14(a). The strong, sharp peak at 694 nm is a well-known emission of Cr³⁺ impurities in the sapphire bulk. An excitation spectrum for this peak is shown in Fig. 4.14(b) over the range all three dyes R6G, R110, and C480, using a sapphire window with relatively high Cr³⁺ content. Multiple features observed in the excitation spectrum are consistent with the absorption spectrum of Cr³⁺ in sapphire at 77 K, including three sharp peaks in the blue, and a broad absorption in the green/yellow with vibrational peaks on the red tail [35, 36]. In addition to the 694-nm peak, a weaker and much broader emission is observed, along with three weak peaks around the 619-nm Ba peak region, also from the sapphire bulk. Excitation spectra for these fluorescence components are shown in Fig. 4.15 for the R6G dye range. In this experiment, the laser was de-focused to about $w = 200 \mu\text{m}$, and the emission observed was from the surface laser spot. As a result, there is contribution of the surface background in the spectrum; this is

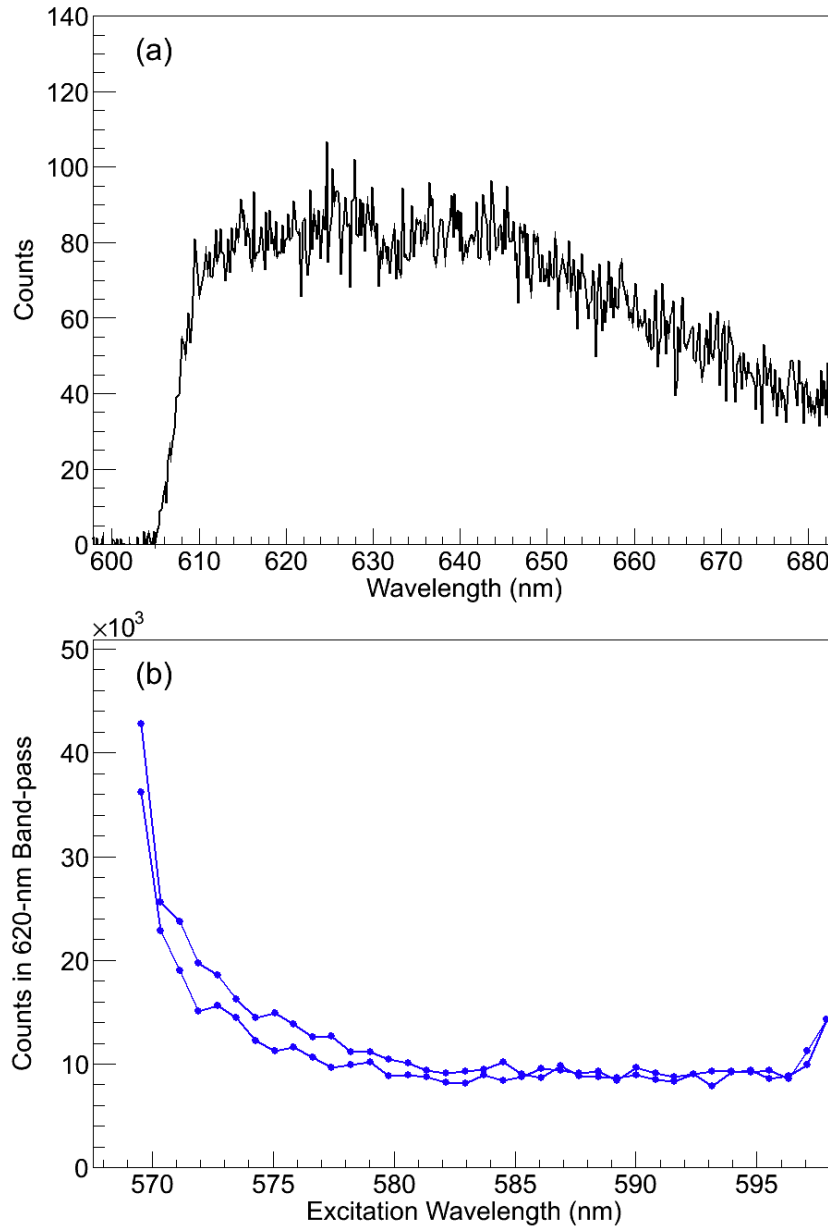


FIGURE 4.12. Surface background emission spectrum w/ excitation at 570.5 nm (a) and its excitation spectrum in R6G dye range (b). The sharp drop in (a) around 608 nm is the Raman filter cutoff.

negligible for the prominent 694-nm peak, however its features, broad excitation with rises near 600 nm and 567 nm, can be seen in the excitation spectra of the weaker components (blue, and especially orange curves in Fig. 4.15). Nonetheless, observation of the same vibrational peaks as in the 694-nm peak demonstrates that the broad emission and weak

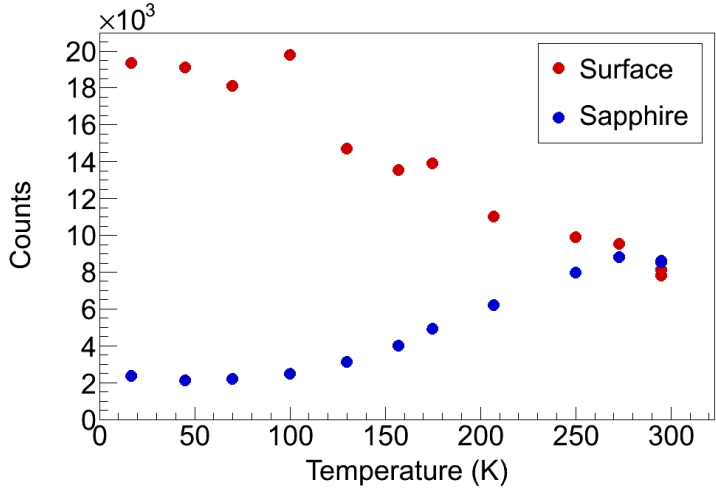


FIGURE 4.13. Temperature dependence of surface (red) and sapphire bulk (b) backgrounds.

peaks in the 620 band-pass (Fig. 4.14(a)) are also due to Cr^{3+} in the sapphire. Commercially available c-plane quality sapphire windows contain very low concentrations of Cr^{3+} . from a few companies were tested, and those from Meller Optics produced the lowest sapphire bulk emission in the 620-nm band-pass region. The choice of 570 nm for excitation of the 619-nm fluorescence peak was made by an optimization of S/\sqrt{B} , where S is the 619-nm signal and the background B is the broad emission in the 620 band-pass filter region (orange curve in Fig. 4.15). The Cr^{3+} emission has an inverse relationship with temperature, shown in Fig. 4.13.

4.6. CANDIDATE Ba^+ LINES/BLUE EXCITATION

Since the fraction of neutralization of Ba^+ deposited in SXe is not known to be 100%, in this system and particularly in future tests of grabbing out of LXe, detection of single Ba^+ in SXe is still of interest. Preliminary studies of fluorescence from Ba^+ deposits were performed by blue laser excitation with the C480 dye laser.

Blue excitation of Ba^+ in SXe were first explored in the thesis of Shon Cook, wherein a set of sharp emission peaks were observed at 522, 575, 637, 712, and 814 nm, in decreasing

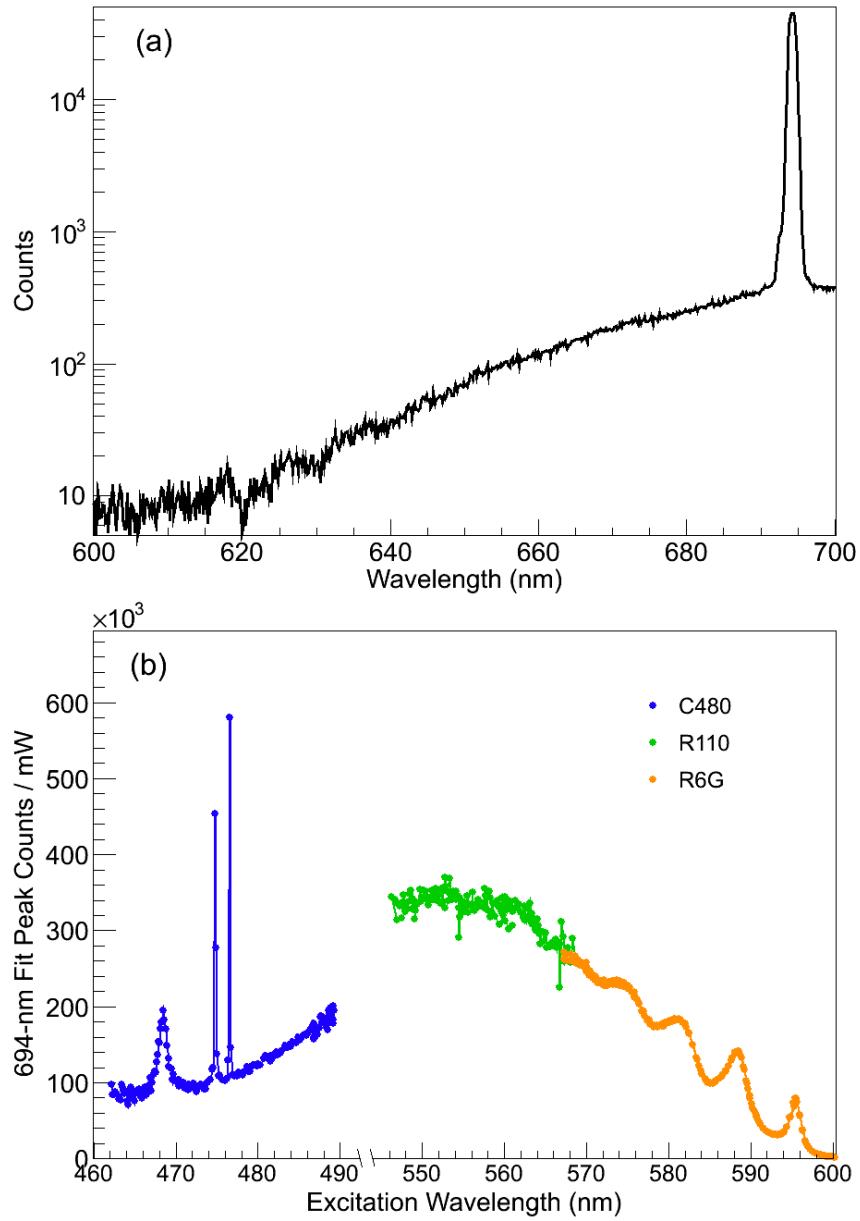


FIGURE 4.14. Sapphire bulk emission with 562-nm excitation at 11 K (a), and excitation spectrum of the sharp 694-nm emission peak using three different laser dyes (b). Relative heights of Coumarin and Rhodamine are not exact, as excitation rates are different between experiments. R110 and R6G were scaled to match at their boundary for the same reason.

amplitude. These peaks were attributed to emission from different vibrational states of a molecule composed of Ba and one or more H atoms [30]. This attribution is supported by two experiments. Firstly, a reduction of those peaks is observed in deposits made at 50 K,

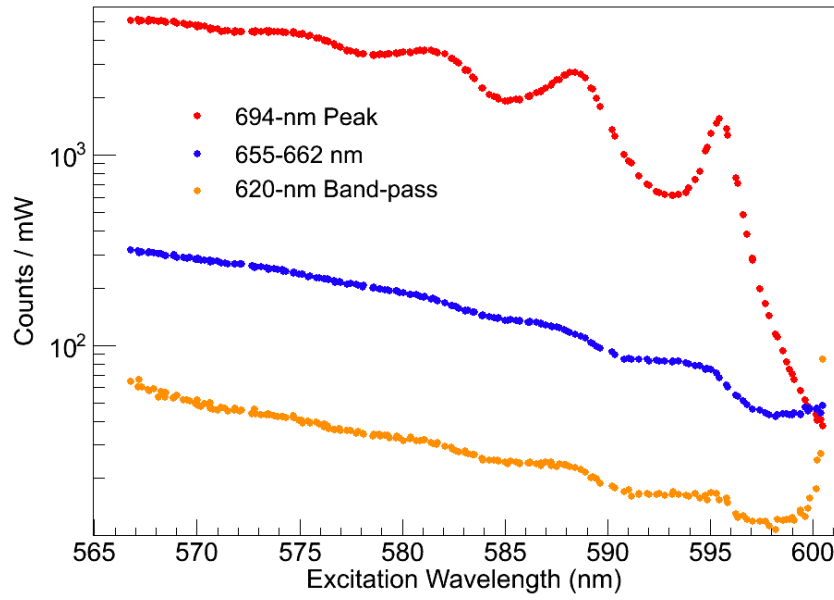


FIGURE 4.15. Excitation spectra for weaker sapphire bulk emissions (blue,orange) along with that of the sharp 694-nm emission (red).

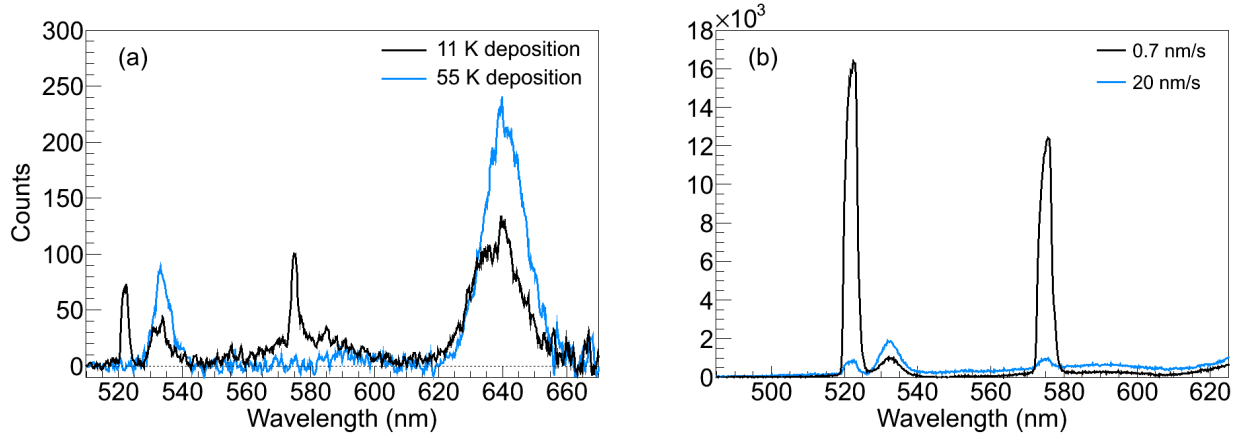


FIGURE 4.16. Comparison of Ba⁺ deposits made at (a) 55 K vs. 11 K, and (b) 20 nm/s vs. 0.7 nm/s.[19]

well above the H₂ freezing temperature of 12 K, vs. deposits made at 11 K, as shown in Fig. 4.16(a). Secondly, the peaks are much stronger in deposits made with lower leak rates, as shown in Fig. 4.16(b), for deposits made at 11 K. This is explained by a higher concentration of H₂ impurities in a matrix formed with a lower leak rate.

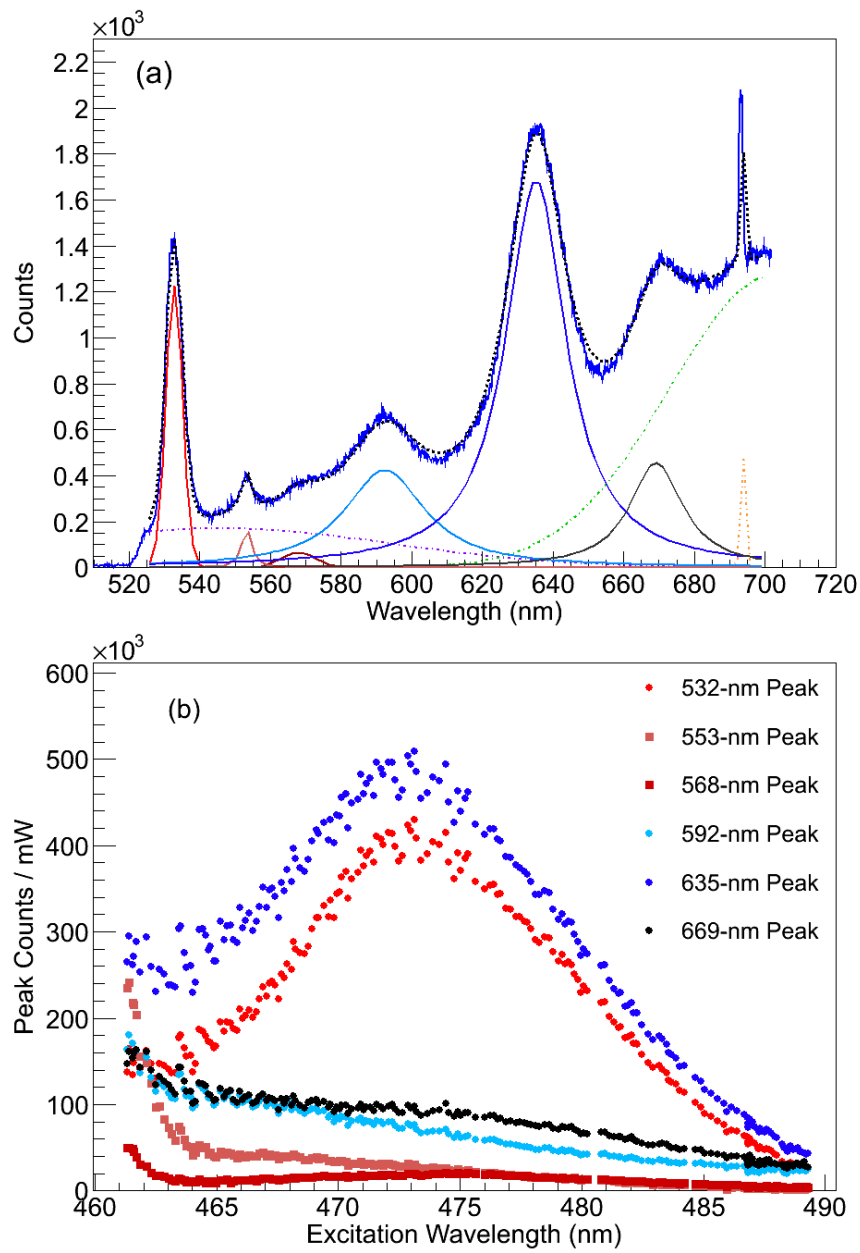


FIGURE 4.17. (a) Multiple-component fit to example emission spectrum with 468.2-nm excitation, and (b) excitation spectra for peaks observed through C480 dye range. In (a), the 532- and 568-nm peaks are fit with Gaussians, and the 553-, 592-, 635- and 669-nm peaks are fit with Lorentzians.

In contrast to lower BaH_x emission, several other emission peaks become prominent in deposits made at 50 ± 5 K and observed at 11 K. A representative spectrum with fits is shown in Fig. 4.17(a), and excitation spectra from those fits over the C480 dye range are shown in Fig. 4.17(b). *The broad blue BG ... what does its excitspec look like? is it possible it*

is the surface BG? ... anyway you need to mention it. Of particular interest are the peaks at 532 nm and 635 nm. These peaks have identical excitation spectra, indicating that they are due to the same excitation transition. Thus the 532- and 635-nm peaks may be due to relaxation to the ground and metastable D states, respectively, from one of the excited P states of Ba⁺ in SXe. However, matrix effects would need to be responsible for the higher number of counts observed in the 635nm peak vs. the 532-nm peak, whereas the P → S transition is about 4× more likely than the P → D transition in vacuum. The resemblance between the excitation spectra for the 592- and 669-nm peaks, as well as between the 553- and 568-nm peaks, is also interesting.

CHAPTER 5

RESULTS: IMAGING

Results presented in Chapter 4 determined the ideal conditions for imaging small numbers of Ba atoms in SXe. Ideal excitation wavelengths were determined by studying the excitation spectra of the signal as well as the background. Bleaching of the fluorescence determined ideal laser intensities to be used. Studies of deposits made and observed at different temperatures informed the procedure of depositing at 50 ± 5 K and observing at 11 K. Imaging of the 577- and 591-nm fluorescence is presented in 5.1 down to the 10^4 -atom level, and imaging of the 619-nm peak is presented down to the single-atom level. Initial scanned images of Ba^+ deposits are presented in 5.3.

Though the imaging spectrometer can produce spacial images with the 0-order grating reflection, better collection efficiency and imaging quality are achieved by removing the spectrometer and imaging directly onto the CCD. Band-pass filters were used to pass the desired Ba fluorescence peak(s) while attenuating laser scatter and sapphire fluorescence.

An example image of the focused 570 nm dye laser passing through a c-plane sapphire window of thickness 0.5 mm, using the 620-nm band-pass filter on the fluorescence, is shown in Fig. 5.1. With $4\times$ magnification, each pixel is $5 \mu\text{m} \times 5 \mu\text{m}$. The laser's path through the window is faintly visible by the tail of the broad Cr^{3+} fluorescence in the 620-nm band-pass. The laser is focused at the top surface of the window, which faces the ion beam. The surface background is seen on both surfaces. The observed size of the laser spot, with a $1/e^2$ radius of about $12 \mu\text{m}$, is larger than the $2.06 \mu\text{m} \times 2.66 \mu\text{m}$ $1/e^2$ laser spot size. Aberrations and vibrations in the collection optics could contribute to this inability to reach the diffraction limit in imaging.

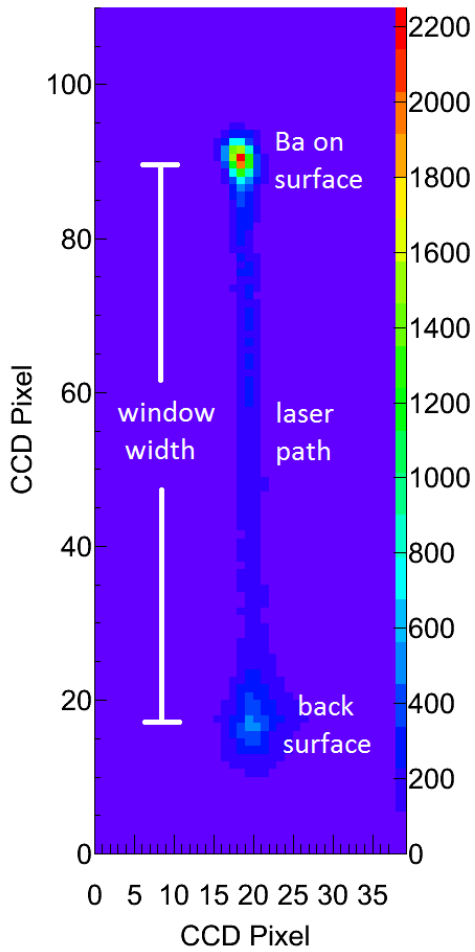


FIGURE 5.1. Example image of focused laser spot on sapphire window surface, and its path through the window. *will replace w/ one w/o Ba*

5.1. IMAGING 577- AND 591-NM PEAKS

First attempts at imaging small numbers of Ba atoms in a focused laser region were done with the 577- and 591-nm Ba fluorescence peaks together using a 586-nm band-pass filter, which passes 573 - 599 nm FWHM. This filter has a 2" diameter, resulting in a factor of 4× more collection efficiency. Bleaching data was used to optimize laser intensity and exposure time to achieve maximal signal in frame 1, and to avoid hole bleaching. The fast bleaching of these peaks is the limiting factor on sensitivity. An image of $\leq 10^4$ atoms (10^4 Ba⁺ ions deposited into the effective laser region) is shown in Fig. 5.2. This is a 100-s exposure with

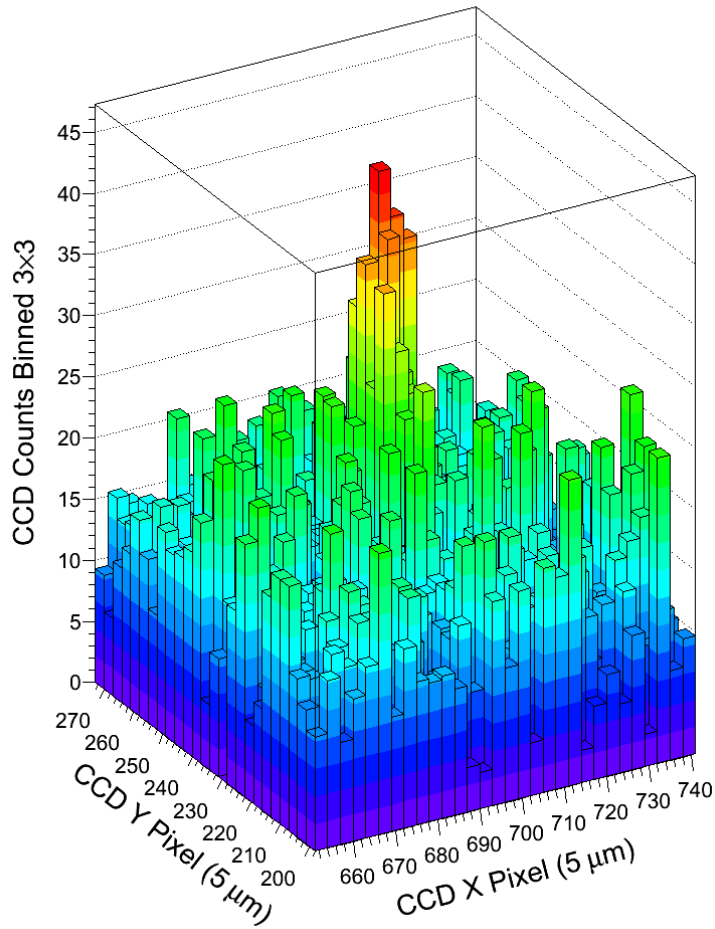


FIGURE 5.2. Image of about 10^4 total Ba atoms in SXe, with about 5×10^3 atoms exposed at a time. 100-s exposure with $.02 \mu\text{W}$ of 566 nm excitation, deposited at 50 K and observed at 11 K. 3×3 CCD pixel binning.

$0.02 \mu\text{W}$ of 566-nm excitation. At this low intensity, no bleaching was observed in the four frames observed (frame 1 is shown). Since the effective laser region is approximately doubled by cryostat vibrations, the signal observed at a given moment in time is actually due to the real laser spot size in the scenario of little to no bleaching. Thus it should be said that Fig. 5.2 is an image of 5×10^3 atoms on average, with 10^4 total atoms exposed. Groups of 9 (3×3) CCD pixels are binned to produce the nice peak shown. As discussed in 4.4, detection of very small numbers of atoms in these sites may require several infrared re-pump lasers. As

a result of low total exposure, neither the sapphire nor the surface backgrounds are present in these images, though a Xe-only image has been subtracted.

5.2. IMAGING 619-NM PEAK

At low laser intensities, the 619-nm peak appears minor compared to the 577- and 591-nm peaks. However, its much lower bleaching rate brings it to dominate over larger exposures, e.g. with the intensity of a focused laser at 0.01-0.1 mW over seconds or minutes. Experiments imaging small numbers of Ba atoms in SXe in a focused laser region with the 619-nm peak were successful down to the single-atom level.

An imaging experiment consisted of many different pulsed Ba^+ deposits, each of which was evaporated after observation. This procedure is described in 3.3-3.5. A linear relationship between observed signal and ions deposited must be observed and repeated. Frequent Xe-only deposits were made, typically every three runs, to establish the local background. The image of each deposit was analyzed by summing the counts of a 3-pixel \times 3-pixel ($15\mu\text{m}\times15\mu\text{m}$) region centered on the laser spot in the SXe layer where it excites Ba atoms, i.e. at the top of the laser path in Fig. 5.1. A partial-bin integrator was implemented such that the 3-pixel \times 3-pixel region could be centered on the peak center of each run, which typically varied by about half a micron between runs. Summed counts vs. Ba^+ ions deposited into the laser region is shown in Fig. 5.3 for a combination of data sets from two separate days *maybe you want them separate (with each point having errors) by color to show agreement*. Each point has subtracted the averaged counts from the two surrounding Xe-only deposits. Some variation in signal is observed, likely due to spatial drifting of the ion beam, as this variation was larger on days where larger beam drift was observed. Nonetheless, a clear linearity is observed in signal vs. ions deposited, all the way down to single ions deposited.

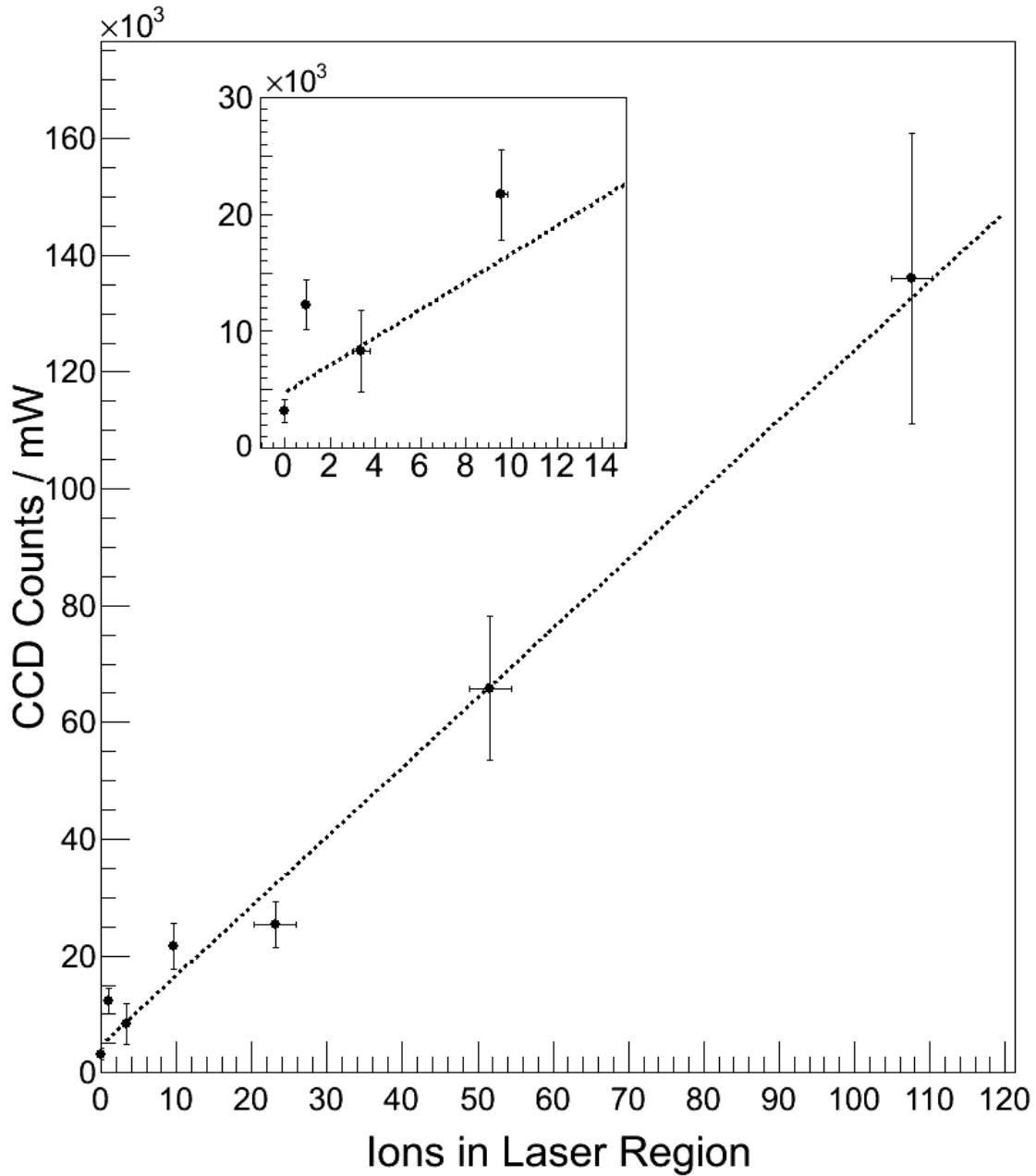


FIGURE 5.3. 619-nm signal vs. Ba^+ deposited in effective excitation region of $17.8 \mu\text{m}$ using focused laser at 570 nm. *move y-ax title over, Remove x errors*

Recall that the number of ions is an upper limit on the number of atoms in the 619-nm peak matrix site. “0-pulse” deposits are also made, wherein Faraday cup 3 is retracted for the

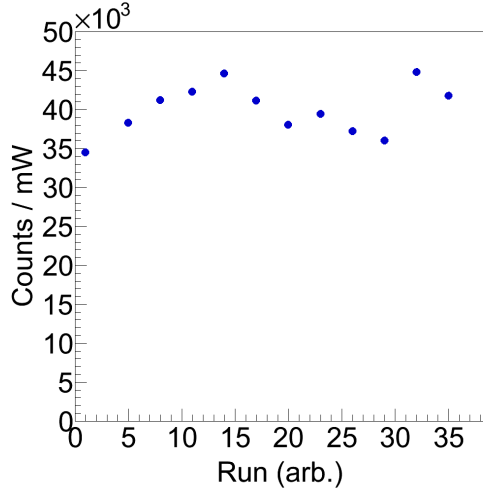


FIGURE 5.4. Background counts in focused laser region over the course of an experiment.

1-s period, but the ion beam remains deflected with no pulses. This establishes the level of neutral Ba atoms making their way down the beam line from the source into the laser region. Signal at the few-atom level is observed from these deposits.

Variation in the background level, dominated by the surface background, is shown in Fig. 5.4. Variation was most likely caused by drift of the laser position on the window, to regions of different historical bleaching. Local variations are at the single-atom signal level, however positive signal after subtraction, even at the single-atom level, demonstrates that this variation is sufficiently low.

Xe-only images were also directly subtracted to produce images of 619-nm Ba fluorescence. In cases where the image has shifted slightly between runs, a binning redistribution was applied to do sub-pixel image shifting for better subtraction, though images which did not require this were preferred. 619-nm fluorescence images for several deposits of varying numbers of atoms are shown in Fig. 5.5.

It is important to note that no Ba signal is left behind after a sample is evaporated, even for large Ba^+ deposits. Raw images (pedestal-subtracted) of Ba^+ deposits and their

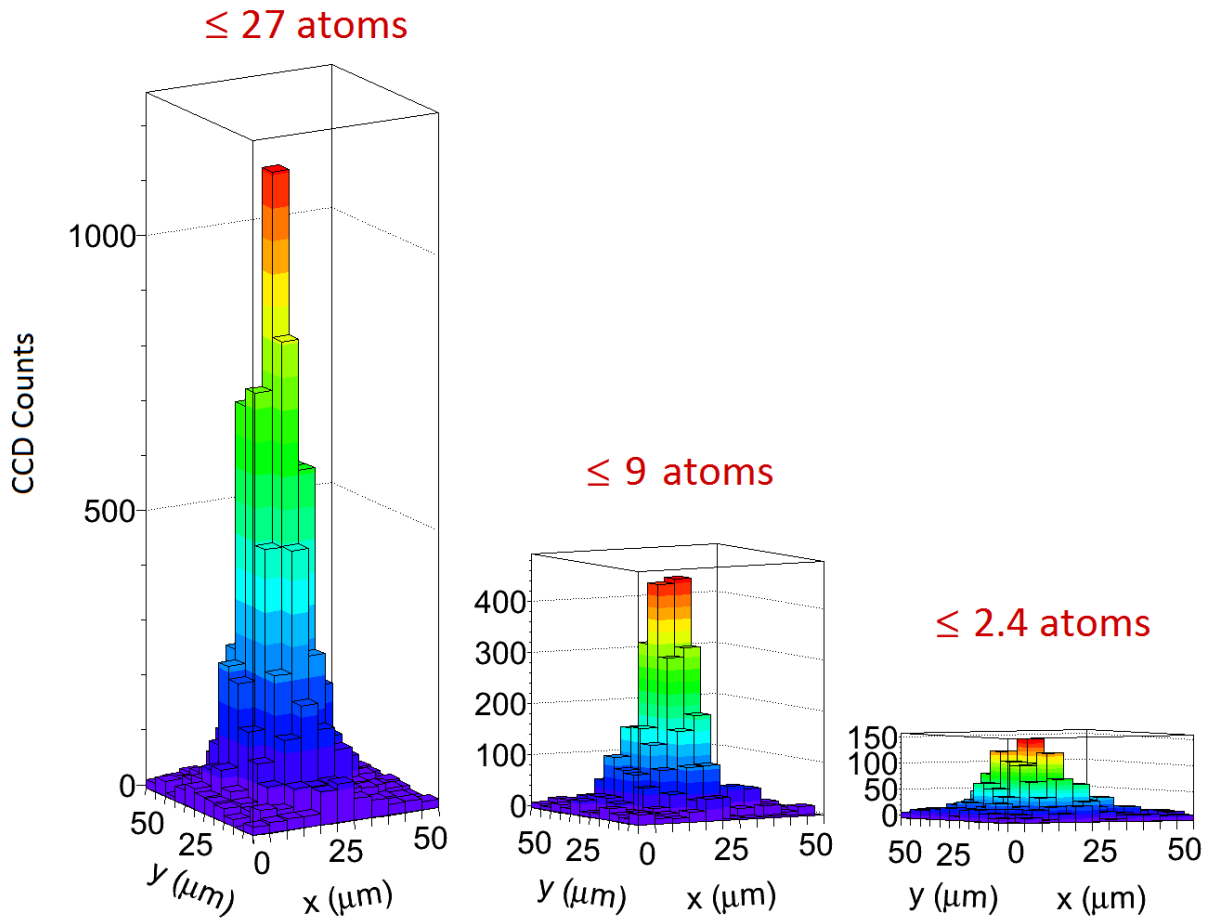


FIGURE 5.5. will change: 1) have more than this, 2) do pixel (5micron) on axis like others, 3) have same-looking phi angle on all

preceding and succeeding Xe-only deposits are shown in Fig. 5.6 for several runs. The lack of historical buildup of Ba is important for the implementation of this method of Ba tagging on a probe in nEXO.

5.3. SCANNED IMAGES

The ultimate demonstration of single-atom imaging would be to scan the focused laser over a sample of separated Ba atoms, observing a peak when the laser moves over each atom. Preliminary scans were performed by scanning the focusing lens in a grid pattern, using the

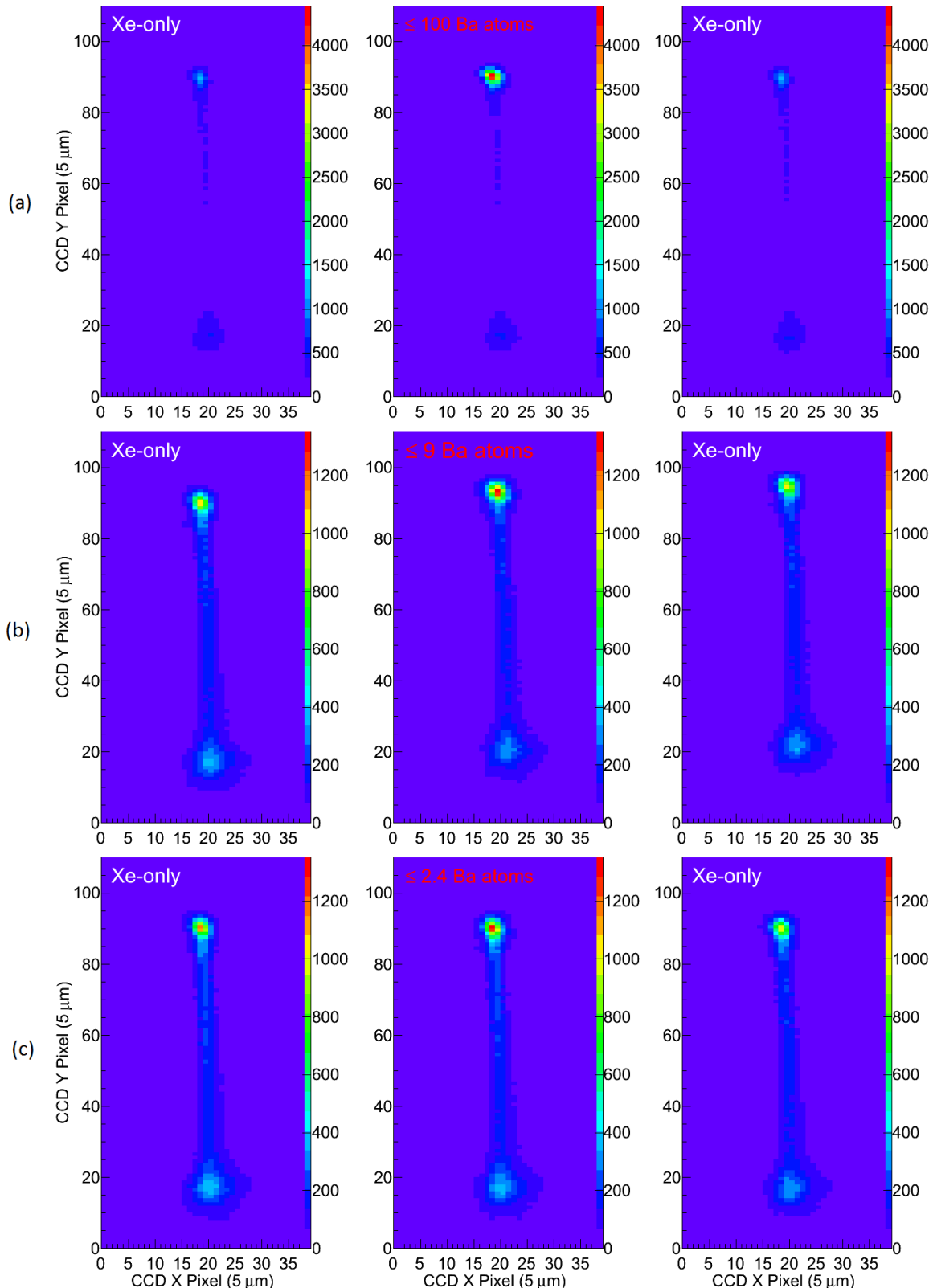


FIGURE 5.6. Raw images of three Ba⁺ deposits yielding (a) ≤ 100 , (b) ≤ 9 , and (c) ≤ 2.4 Ba atoms, with their preceding and succeeding Xe-only deposits.

setup described in 3.7. choose what to show and what to say about it – there are some decent things to show really [issues are BG, reproduceability, vibrations]

CHAPTER 6

CONCLUSIONS

6.1. FUTURE STEPS

Talk about whatever Chris will do next ... ions? Other sites? Populations?

Talk about Adam's work, show pics and stuff.

BIBLIOGRAPHY

- [1] C.D. Ellis and W.A. Wooster, “The average energy of disintegration of radium e,” *Proceedings of the Royal Society (London)* **A117** 109-123 (1927).
- [2] F. Wilson, *American Journal of Physics* **36**, 12 (1968).
- [3] Y. Fukuda *et al.* (Super-Kamiokande Collaboration), *Phys. Rev. Lett.* **81** 1562 (1998).
- [4] S.T. Petcov, W. Rodejohann, T. Shindou, Y. Takanishi, *Nuclear Physics B* **739**, 208233 (2006).
- [5] M. Danilov *et al.*, *Physics Letters B* **480**, 1218 (2000).
- [6] K.A. Olive *et al.* (Particle Data Group), “14. Neutrino Mass, Mixing, and Oscillations,” *Chin. Phys. C* **38**, 090001 (2014) (<http://pdg.lbl.gov>)
- [7] P.A.R. Ade *et al.* (Planck Collaboration), *Astronomy and Astrophys.* **571**, A16 (2014).
- [8] N. Steinbrink *et al.*, *New Journal of Physics* **15**, 113020 (2013).
- [9] J. Albert *et al.* (EXO-200 Collaboration), *Phys. Rev. C* **89**, 015502 (2014).
- [10] M. Moe, *Phys. Rev. C* **44**, R931 (1991).
- [11] M. Auger *et al.*, *JINST* **7**, P05010 (2012).
- [12] R. Nielson *et al.*, *Nuclear Instruments and Methods in Physics Research A* **608**, 68 (2009).
- [13] E. Conti *et al.*, *Phys. Rev. B* **68**, 054201 (2003).
- [14] J. Albert *et al.* (EXO-200 Collaboration), *Nature* **510**, 229 (2014).
- [15] N. Ackerman *et al.* (EXO-200 Collaboration), *Phys. Rev. Lett.* **107**, 212501 (2011).
- [16] A. Gando *et al.* (KamLAND-Zen Collaboration), *Phys. Rev. C* **86**, 021601 (2012).
- [17] K. Hall, *In-situ Laser Tagging of Barium Ions in Liquid Xenon for the EXO Experiment*. Colorado State Universtiy Thesis/Dissertation (2012).
- [18] K. Twelker *et al.*, *Review of Scientific Instruments* **85**, 095114 (2014).

- [19] B. Mong *et al.*, *Phys. Rev. A* **91**, 022505 (1954).
- [20] T. Brunner *et al.*, *International Journal of Mass Spectrometry* **379**, 110-120 (2015).
- [21] J. J. Curry, *Journal of Physical and Chemical Reference Data* **33**, 725 (2004).
- [22] A. Mohanty *et al.*, *Hyperfine Interactions* **233**, 113-119 (2015).
- [23] N. Yu, W. Nagourney, H. Dehmelt, *Phys. Rev. Lett.* **78**, 26 (1997).
- [24] S. De, U. Dammalapati, K. Jungmann, L. Willmann, *Phys. Rev. A* **79**, 041402(R) (2009).
- [25] M. Green *et al.*, *Phys. Rev. A* **76**, 023404 (2007).
- [26] E. Whittle, D. Dows, G. Pimentel, *The Journal of Chemical Physics* **22**, 1943 (1954).
- [27] C. Crepin-Gilbert and A. Tramer, *Int. Reviews in Physical Chemistry* **18**, No. 4, 485-556 (1999).
- [28] L. C. Balling and J. J. Wright, *The Journal of Chemical Physics* **83**, 5 (1985).
- [29] L. W  hlin, “The Colutron, a Zero Deflection Isotope Separator,” *Nuclear Instruments and Methods* **27** 55-60 (1964).
- [30] S. Cook, *Detection of Small Numbers of Barium Ions Implanted in Solid Xenon for the EXO Experiment*. Colorado State Universtiy Thesis/Dissertation (2012).
- [31] B. Mong, *Barium Tagging in Solid Xenon for the EXO Experiment*. Colorado State Universtiy Thesis/Dissertation (2011).
- [32] A. C. Sinnock, *J. Phys. C: Solid St. Phys.* **13**, 2375-91 (1980).
- [33] Tache, J.-P., *Applied Optics* **26**, 429 (1987).
- [34] D. Richard Sears, Harold P. Klug, *The Journal of Chemical Physics* **37**, 12 (1962).
- [35] R. A. Ford, O. F. Hill, *Spectrochimica Acta* **16**, 493-496 (1960).
- [36] D. S. McClure, *Solid State Phys.* **9**, 399-525 (1959).